The Version-2 Global Precipitation Climatology Project (GPCP) Monthly Precipitation Analysis (1979–Present)

ROBERT F. ADLER,* GEORGE J. HUFFMAN,+ ALFRED CHANG,# RALPH FERRARO,@ PING-PING XIE,& JOHN JANOWIAK,& BRUNO RUDOLF,** UDO SCHNEIDER,** SCOTT CURTIS,++ DAVID BOLVIN,+ ARNOLD GRUBER,@ JOEL SUSSKIND,* PHILIP ARKIN,## AND ERIC NELKIN+

*Laboratory for Atmospheres, NASA GSFC, Greenbelt, Maryland
+Laboratory for Atmospheres and Science Systems and Applications, Inc., NASA GSFC, Greenbelt, Maryland
#Laboratory for Hydrospheric Processes, NASA GSFC, Greenbelt, Maryland
@NOAA/NESDIS Office of Research and Applications, Camp Springs, Maryland
&NOAA/NWS/National Centers for Environmental Prediction, Camp Springs, Maryland
**Global Precipitation Climatology Center, Deutscher Wetterdienst, Offenbach, Germany
++Laboratory for Atmospheres and University of Maryland, Baltimore County, Baltimore, Maryland
##University of Maryland, College Park, College Park, Maryland

(Manuscript received 13 November 2002, in final form 23 April 2003)

ABSTRACT

The Global Precipitation Climatology Project (GPCP) Version-2 Monthly Precipitation Analysis is described. This globally complete, monthly analysis of surface precipitation at 2.5° latitude × 2.5° longitude resolution is available from January 1979 to the present. It is a merged analysis that incorporates precipitation estimates from low-orbit satellite microwave data, geosynchronous-orbit satellite infrared data, and surface rain gauge observations. The merging approach utilizes the higher accuracy of the low-orbit microwave observations to calibrate, or adjust, the more frequent geosynchronous infrared observations. The dataset is extended back into the premicrowave era (before mid-1987) by using infrared-only observations calibrated to the microwave-based analysis of the later years. The combined satellite-based product is adjusted by the rain gauge analysis. The dataset archive also contains the individual input fields, a combined satellite estimate, and error estimates for each field. This monthly analysis is the foundation for the GPCP suite of products, including those at finer temporal resolution. The 23-yr GPCP climatology is characterized, along with time and space variations of precipitation.

1. Introduction

Precipitation information is critical in understanding the hydrologic balance on a global scale and in understanding the complex interactions among the small- and large-scale components within the hydrologic cycle. The latent heating associated with precipitation is a primary atmospheric energy source and knowledge of the spatial and temporal distribution of precipitation around the globe is crucial for improving climate diagnostics and improving weather and climate forecast models. The distribution of precipitation is also important for water management for agriculture, electrical power and flood control, and for drought and flood monitoring. A better understanding of the global and regional hydrologic cycles is at the heart of the World Climate Research Program (WCRP) and its key Global Energy and Water Cycle Experiment (GEWEX) component. The Global Precipitation Climatology Project (GPCP) is the WCRP GEWEX project devoted to producing community analyses of global precipitation.

The GPCP is an international project with input datasets and techniques being contributed to the monthly analysis by a number of investigators. Version 1 of the GPCP monthly dataset was described by Huffman et al. (1997), and this paper describes the improved, time-extended Version 2 of the dataset. The description focuses on new datasets and techniques used in Version 2, differences between the old and new analyses, and examples of applications.

The GPCP's present goal is to provide a long time series of monthly and finer time resolution precipitation analyses on a global scale. The primary product is a monthly analysis on a global 2.5° latitude × 2.5° longitude grid for the period 1979–present, which is the subject of this paper. A second product is a pentad (5 day) global analysis adjusted by the monthly analysis, described by Xie et al. (2003). A third product is a daily, 1° latitude × 1° longitude analysis from 1 January 1997 to the present, as described by Huffman et al. (2001), also constrained by the monthly analysis. This suite of coordinated products provides the re-

Corresponding author address: Dr. Robert F. Adler, Laboratory for Atmospheres, NASA GSFC, Code 912, Greenbelt, MD 20771.
E-mail: robert.f.adler@nasa.gov

© 2003 American Meteorological Society

search community with global precipitation information useful for a large number of applications. These products are archived and distributed through World Data Center A at the National Oceanic and Atmospheric Administration (NOAA) National Climatic Data Center. (They can be accessed online at http://lwf.ncdc.noaa.gov/oa/wmo/wdcamet-ncdc.html, and are also available at http://precip.gsfc.nasa.gov and http://gpcc.dwd.de/.)

The GPCP monthly dataset described in this paper is similar in form to that of Xie and Arkin (1997), although the analysis methodologies are different. A comparison of that product to the older Version-1 GPCP dataset is given by Gruber et al. (2000). A recent comparison of many satellite-based estimates of global precipitation, including the GPCP product, is described by Adler et al. (2001).

The general approach with the new GPCP monthly product is to combine the precipitation information available from each source into a final merged product, taking advantage of the strengths of each data type and removing biases based on hierarchical relations in the stepwise approach. The microwave estimates are based on Special Sensor Microwave Imager (SSM/I) data from the Defense Meteorological Satellite Program (DMSP, United States) satellites, which fly in sun-synchronous low-Earth orbits. The infrared (IR) precipitation estimates are obtained primarily from geostationary satellites operated by the United States, Europe, and Japan, and secondarily from polar-orbiting satellites. Additional precipitation estimates are obtained based on Television and Infrared Observation Satellite (TIROS) Operational Vertical Sounder (TOVS) and outgoing longwave radiation (OLR) measurements. Rain gauge data are collected, quality controlled, and analyzed to contribute to the analysis over land.

2. Input datasets

This section describes the input datasets that are used in Version 2 of the GPCP monthly analysis. Most of the datasets used in Version 2 were also used in Version 1 and were described in Huffman et al. (1997). Only a brief summary will be given here (section 2a) and the reader is referred to the earlier paper for details on those datasets. The additional datasets that have contributed to Version 2 are described in section 2b.

a. Datasets utilized in Versions 1 and 2

1) GPCC RAIN GAUGE ANALYSES

For the period 1986 to the present, the monthly rain gauge analyses are constructed by the Global Precipitation Climatology Centre (GPCC) operated by the German Weather Service. The GPCC uses a variant of the spherical-coordinate adaptation of Shepard's method (Willmott et al. 1985) to interpolate the station data to regular grid points (0.5° latitude × 0.5° longitude mesh). These regular points are then averaged to provide area mean, monthly total precipitation on 2.5° grid cells. The Version-2 rain gauge product is based on about 6500–7000 rain gauge stations worldwide, mostly synoptic and monthly climate reports collected from the Global Telecommunications Network in real time, supplemented by other worldwide data collections, such as the Monthly Climatic Data for the World.

Sophisticated quality control is performed before carrying out the analyses. First, station metainformation (especially location) is checked. The precipitation data themselves are checked for coding, typing, or transmission errors. In addition, they are checked automatically for spatial homogeneity, compared to climatological normals, and are intercompared among different sources of data. Precipitation data flagged as questionable in the automatic process are then checked manually by an expert at a graphics workstation, where 3D orography and other background fields can be overlaid, and orographic conditions can be taken into consideration.

Precipitation measurements from rain gauges are also affected by systematic errors, primarily losses due to aerodynamic effects, especially with snow. We apply an estimate of systematic error using bulk correction factors for monthly climatological conditions as derived by Legates (1987), based on work summarized by Sevruk (1989). An improved method taking into account the day-to-day variations of the weather conditions during the current month is in preparation (Fuchs et al. 2001; Ungersböck et al. 2000). A general description of the GPCC data-processing and analysis system is given by Rudolf (1993). Details on the sampling error and availability of data are discussed by Rudolf et al. (1994, 1998).

2) MICROWAVE EMISSION ESTIMATES OVER OCEAN

The microwave estimates over the ocean utilize data from the SSM/I instruments and the Wilheit et al. (1991) histogram approach in which the rain rate is modeled as a mixed distribution, made up of a discrete probability of no rain and a lognormal distribution for rain events, and related to brightness temperature (T_b) histograms using a combination of 19- and 22-GHz channels. The height of the freezing level, which is needed by the radiative transfer calculation, is estimated empirically using the brightness temperatures themselves. The resulting SSM/I rain-rate estimates are multiplied by a coefficient to account for the beam-filling bias (Wilheit et al. 1991; Chiu et al. 1993). The coefficient ($1 + 0.062 \times \mathrm{FL}$) is a function of freezing level (FL). The microwave emission estimates are computed by the Laboratory for Hydrospheric Processes at the National Aeronautics and Space Administration (NASA) Goddard Space Flight Center (GSFC).

3) MICROWAVE-SCATTERING ESTIMATES OVER LAND

The primary GPCP-scattering algorithm is an 85-GHz technique based on the Grody (1991) scattering index (SI) applied to SSM/I data, most recently described by Ferraro (1997). It has separate components for land and ocean, as well as screening tests for the removal of artifacts caused by various surface types. The coastline is thickened by 50 km, and the land component is applied over both land and the ''coast.'' The algorithm has been calibrated to instantaneous rain rates from ground-based radar measurements (Ferraro and Marks 1995). Recent efforts have focused on the development of error estimates to accompany the rain estimates (Li et al. 1998, 2000) and further evaluate the error characteristics (McCollum et al. 2002). For the period from June 1990 to late 1991, failure of the 85-GHz channels on the operational SSM/I instrument led to the use of a secondary scattering algorithm using the 37-GHz SI information. While the 85-GHz SI technique can detect rain rates as low as 1 mm h^{-1}, the 37-GHz SI is only sensitive to rain rates of 5 mm h^{-1} or greater. The monthly scattering-based rainfall field is computed by the Office of Research and Application (ORA) of the NOAA National Environmental Satellite, Data, and Information Service (NESDIS). The ocean and land microwave estimates are merged in the near-coastal areas based on relative sampling as described in Huffman et al. (1997).

4) GEOSYNCHRONOUS IR-BASED ESTIMATES

The geosynchronous IR-based estimates employ the Geostationary Operational Environmental Satellite (GOES) Precipitation Index (GPI; Arkin and Meisner 1987) technique, which relates cold cloud-top area to rain rate. The data are generated by each cooperating geostationary satellite operator [GOES, United States; the Geosynchronous Meteorological Satellite, (GMS), Japan; and the Meteorological Satellite (Meteosat), European Community]. The data for the period 1986–96 are accumulated every 3 h into 16-class histograms of IR T_b on a 2.5° latitude × 2.5° longitude grid in the zone 40°N–40°S and saved for each pentad of days (1–5 January, 6–10, . . . , 27–31 December). Separate histograms are accumulated for each 3-h period of the day (0000, 0003 UTC, 2100 UTC), which preserves the mean diurnal cycle for each pentad. Starting in 1997 the data collection was modified to increase the resolution to a 1° latitude × 1° longitude grid, with data every 3 h of each day, instead of pentads. The geosynchronous IR data are corrected for viewing geometry and intersatellite calibration effects, based on the work of Joyce and Arkin (1997). The global IR rainfall estimates are then generated from a merger of these data at the Climate Prediction Center (CPC) of NOAA using the GPI. In cases where geostationary data are unavailable, data from Advanced Very High Resolution Radiometer (AVHRR) on the NOAA polar-orbiting satellites are used either in the form of T_b histograms or the integrated value of OLR, depending on available historical data. These fields are converted to GPI estimates using the procedures of Janowiak and Arkin (1991). Depending on the satellites contributing, the polar-orbit data provide from zero to four images per day, never more than half the samples available from the geostationary data.

b. Additional datasets used in Version 2

1) GHCN–CAMS GAUGE ANALYSIS

During the pre-GPCC period, January 1979–December 1985, the rain gauge analysis precipitation product used is a combination of rain gauge data from the Global Historical Climate Network (GHCN) (produced by NOAA/National Climate Data Center) and Climate Assessment and Monitoring System (CAMS) (produced by the CPC, National Centers for Environmental Prediction, and NOAA), and is analyzed using the same variant of Shephard's method that GPCC uses. The combined GHCN–CAMS gauge analyses for this period were produced by the NOAA CPC group, using procedures described by Xie et al. (1996). This analysis includes error checking based on station availability. The same corrections for systematic error due to wind effects, etc., used with the GPCC gauge dataset have been applied to this dataset also.

2) TOVS-BASED ESTIMATES

The TOVS precipitation product uses data from the TOVS instruments aboard the NOAA series of polar-orbiting platforms. A number of meteorological variables are retrieved or estimated from the TOVS data, including precipitation (Susskind and Pfaendtner 1989; Susskind et al. 1997). The technique infers precipitation from deep, extensive clouds using a regression relationship between collocated rain gauge measurements and several TOVS-based parameters that relate to cloud volume: cloud-top pressure, fractional cloud cover, and relative humidity profile. The TOVS retrieval utilizes output from a general circulation model as part of the first guess for the moisture retrieval, which in turn is used in the precipitation estimate. This relationship is allowed to vary seasonally and with latitude. Furthermore, separate relationships are developed for the ocean and land. The TOVS precipitation estimates are routinely produced by the Laboratory for Atmospheres of NASA's GSFC.

The TOVS data are used for the SSM/I period (July 1987–present) and are provided at the 1° spatial and monthly temporal resolution. The data covering the span July 1987–February 1999 are based on information from two satellites. For the period March 1999–present, the TOVS estimates are based on information from one sat-

ellite due to changes in satellite data format. A future release should include data from both NOAA satellites.

During the SSM/I period, the TOVS estimates are used for filling in data voids—the polar and cold-land regions for which SSM/I-based estimates are unavailable due to shortcomings in retrieving precipitation information over frozen surfaces. In the span 40°N–40°S, the SSM/I data are used as is. Where there are holes as the result of cold land, the TOVS data are adjusted to the zonally averaged mean bias of the SSM/I data and inserted. Just outside of the zone 40°N–40°S, the SSM/I and TOVS data are averaged using equal weighting. Moving further toward the poles, the SSM/I data become progressively less reliable, and the SSM/I–TOVS average is replaced with zonally averaged, bias-adjusted TOVS data. The bias adjustment is anchored on the equatorial side by the SSM/I–TOVS average and on the polar side by climatological rain gauge estimates. From 70°N to the North Pole, TOVS data are adjusted to the bias of the available monthly rain gauge data. From 70°S to the South Pole, TOVS data are adjusted to the bias of the annual average climatology of the rain gauge data. The monthly climatological values are not used in the Antarctic because the lack of sufficient gauge coverage there yields unstable results. The end result is a globally complete SSM/I–TOVS precipitation field based on the polar orbiters, with preference given to the microwave estimates, where available.

3) OLR PRECIPITATION INDEX (OPI)

The OPI technique (Xie and Arkin 1998) is based on the use of low-Earth-orbit satellite OLR observations. Lower OLR radiances are directly related to higher cloud tops, which are related to increased precipitation rates. It is necessary to define radiance anomalies locally, so OLR and precipitation climatologies are computed and a regression relationship is developed between OLR anomalies and precipitation anomalies. In use, the total precipitation inferred is the estimated anomaly plus the local monthly climatological value. A backup direct OLR–precipitation regression is used when the anomaly approach yields physically unrealistic values. For use as part of the GPCP the OPI estimates are calibrated against the globally complete GPCP estimates from 1988–98. During the pre-SSM/I period of January 1979–June 1987 and December 1987, the OPI data, calibrated by the GPCP satellite–gauge estimates for the SSM/I period, are used as a replacement for the multisatellite estimates. The OPI estimates calibrated by the GPCP analyses are produced routinely by the CPC.

c. *Error estimates*

The error estimates for the input fields and combination products are based on Huffman (1997) and Huffman et al. (1997). The estimates are for random error (bias error is assumed to be removed in the analysis procedure) and include both algorithm and sampling random errors. The work is based on seeking to parameterize σ^2, the (random) error variance that remains when we compute $\bar{r}$, the average precipitation rate, in a grid box from a finite set of observations (N samples). When the samples are sparse in space (gauges) or time (satellites), σ^2 may be approximated simply from the accumulated histogram of individual precipitation rates that contribute to $\bar{r}$, including zeroes. The key step is that the summation over the histogram on which σ^2 depends can be nondimensionalized and labeled H, which turns out to have a very narrow range of values for typical precipitation histograms. After several approximations, the final form of the relation for σ^2 is

$$\sigma^2 \cong \frac{H(\bar{r} + S)}{IN}[24 + 49\sqrt{\bar{r}}], \qquad (1)$$

where S is introduced to account for $\sigma^2(\bar{r} = 0) \neq 0$, I is a multiplicative factor approximately relating N to the number of independent samples in the histogram, and the term in the square brackets is an empirical parameterization of the probability of precipitation in terms of $\bar{r}$, based on examination of satellite estimates and gauge analyses; H/I and S are taken to be constant and then set for each of the input single-source datasets by comparison against gauge data. Note that this calibration is most applicable when the local sampling and climatology are similar to those in the calibration area. Once the error estimates are calculated, they can provide weights for the combination procedure, and the users of both the input products and combined analyses have information with which to judge the utility of the dataset for their particular application.

3. Combination methods

The merging techniques used for the GPCP monthly product are different for the SSM/I period of 1987 to the present and for the 1979 to 1987 period when no microwave-based estimates were used. A block diagram of the product generation is shown in Fig. 1.

a. *Combination method for 1987–present*

For the 1987–present period, during which SSM/I data are available, the combination method is very similar to that described in Huffman et al. (1997). It is designed to use the strengths of each input dataset to produce merged global, monthly precipitation fields that are superior to any of the individual datasets. The technique is also designed to reduce bias in each step by using the input original or intermediate product with the presumed smallest or zero bias to adjust the bias of other products. For example, microwave-based estimates are presumed to have lower biases than IR-based estimates, and gauges are presumed to be unbiased relative to the combination of satellite estimates over land.

A key feature of the GPCP merge technique has cen-

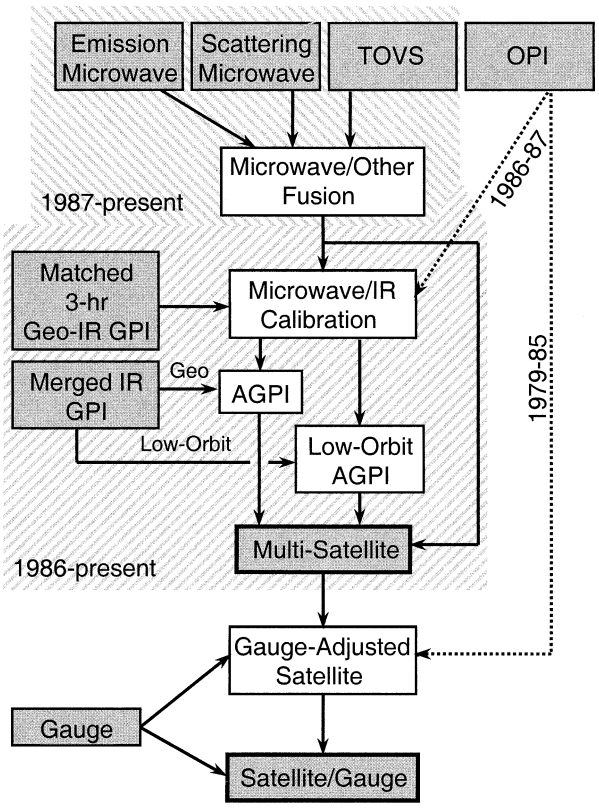

FIG. 1. Block diagram of the Version-2 satellite–gauge (SG) precipitation combination technique. Shaded boxes with thin borders are input datasets, shaded boxes with thick borders are output datasets produced in the SG, and unshaded boxes are intermediate datasets produced in the SG. Arrows show data flow. Hatched background and dotted arrows indicate the years for which various parts of the computation are done, as described in the text.

tered on combining the superior physical basis of the microwave-based observations from a low-orbit satellite and the frequent time sampling of the geosynchronous IR observations. Adler et al. (1991, 1993) described a technique for using precipitation estimates from low-orbit microwave data to ''adjust'' GPI precipitation estimates made from geosynchronous IR data. The resulting ''microwave-adjusted IR'' estimates provide an objective means of correcting known biases in the geosynchronous IR estimates, while retaining the high sampling rate of the geosynchronous satellite. This approach was then adapted to be applied on a global, tropical basis, as described by Adler et al. (1994), and by the GPCP (Huffman et al. 1997). First, for each month the microwave estimates are approximately time and space matched with geosynchronous IR GPI estimates to derive additive and multiplicative microwave/IR calibration factors (see Fig. 1). In regions lacking geosynchronous IR data, rainfall estimates from the NOAA polar-orbiting satellites are adjusted using a smoothly varying interpolation of the microwave/geosynchronous IR adjustment ratio. The spatially varying arrays of adjustment coefficients are then applied to the full month of GPI estimates, producing the adjusted GPI (AGPI) precipitation field, which has the desirable, 3-h sampling of the geosynchronous data and the typically small bias of the instantaneous microwave estimates. Verification against rain gauge analyses over water and land, and subjective examination of the resulting maps and zonally averaged fields indicate that known biases in the GPI in the subtropics and over land are reduced using this adjustment approach (Adler et al. 1993, 1994).

The GPCP Version-2 merging procedure introduces TOVS-based estimates to fill in the high latitudes, where SSM/I-based estimates are unavailable or unreliable. Equatorward of seasonally varying latitude boundaries (about 40°–50°N and 40°–50°S, chosen by inspection of monthly climatological zonal profiles) the microwave data is used by itself. Poleward of 70°N and 70°S the TOVS is adjusted based on a comparison of TOVS and climatological gauge values. In the midlatitudes an average of TOVS and SSM/I is used, with a smooth transition over 60°–70°N and 60°–70°S to the gauge adjustment at 70°N and 70°S. Areas lacking SSM/I equatorward of 60°N and 60°S (generally over land) are filled with TOVS, adjusted by the ratio of zonal average SSM/I (or SSM/I–TOVS average) and TOVS.

A multisatellite precipitation product is formed of AGPI, between 40°N and 40°S, and SSM/I and TOVS values elsewhere. In areas of the Tropics where geosynchronous data are unavailable (e.g., the Indian Ocean) microwave-adjusted low-orbit IR is combined with SSM/I estimates.

Next, the large-scale (5×5 grid box) average of the multisatellite analysis is adjusted to agree with the large-scale average of the gauges (over land and where available). This keeps the bias of the satellite and gauge combination close to the (presumably small) bias of the gauge analysis on a regional scale. Finally, the gauge-adjusted, multisatellite estimate and the gauge analysis are combined with inverse-error–variance weighting to produce the final, merged analysis. This gauge–satellite combination approach allows the multisatellite estimate to provide important local variations in gauge-sparse areas, while still retaining the overall gauge bias. The efficacy of this procedure was demonstrated by McCollum et al. (2000) in their study of biases in satellite estimates relative to gauges over equatorial Africa.

Random error fields are computed for each of the underlying fields and the final product. As outlined in section 2c for underlying fields, the nominal error depends on the particular field (e.g., microwave), and fluctuations depend on sampling and rain amount. The theoretically based functional form currently used was derived in Huffman (1997) and validated by Krajewski et al. (2000). Random error estimates for the satellite–gauge combination are computed in the combination step.

b. Combination method for 1979–87

The GPCP analysis is extended back to 1979 using the OPL (Xie and Arkin 1998) trained against a con-

current period of the GPCP-merged dataset. The OPI was developed based on the observation that, while the mean annual cycle of OLR (calculated using the NOAA AVHRR data stream) reflects both the surface temperature and cloudiness, OLR *anomalies* have a clear negative correlation with precipitation *anomalies* over most of the globe. This information was used to develop regression coefficients that relate OLR anomalies to precipitation. While these coefficients are spatially inhomogeneous and seasonally varying, they can be expressed rather accurately as a globally uniform linear function of the local mean precipitation anomalies. The precipitation anomalies are computed from the OLR anomaly relationship and then added to base period mean values to generate monthly precipitation accumulations. In this application the OPI is trained against the GPCP-merged analysis for the 1988–97 period. The OPI relations developed with the GPCP dataset are then applied to the OLR anomalies for the 1979–85 period to produce the monthly OPI-based precipitation estimates. The OPI estimates take the place of the SSM/I and geosynchronous estimates for this early period, and are then merged with the gauge analysis over land as in the later period.

4. Results

a. Example month

Figure 2 (top panel) shows an example of the GPCP monthly merged final product, in this case for February 2001. The general rainfall patterns for this month are typical of Northern Hemisphere winter months. Over southeast Africa a maximum of precipitation (20 mm day^{-1}) is associated with the devastating floods that occurred there at this time. The middle panel of Fig. 2 has the random error field associated with the merged monthly estimate. The error estimate includes both error due to the algorithm and sampling error. The pattern closely follows the rain field in the top panel due to the close relation of the error to the estimated rain as indicated in Eq. (1). This relation can be seen in Fig. 3, which shows the relation between estimated error and rain rate for this month, with each point representing the result for a 2.5° square. The general increase of error with rain rate can be seen, but there is fairly large scatter. However, there are also identifiable curves formed by collections of points that relate to particular regions that contain the same combination of input data. The collection of points extending out to the letter A in the diagram is for ocean areas in the 40°N–40°S area where both SSM/I and geosynchronous IR data are used. The sampling provided by the IR data lowers the random error, as compared to the ocean areas outside latitude 40°, which have only the sampling of a single SSM/I, and are indicated by B in Fig. 3. The letter C denotes the near end point of a collection of points over land, which have a generally lower error due to the gauge input (in addition to satellite), but have significant error variability due to the variation in number of gauges in each box. Overall the errors range between 10%–30% at rain amounts above 100 mm month^{-1} (3 mm day^{-1}). This percentage error is for a 2.5° latitude × 2.5° longitude square, and time and space averaging will significantly reduce the estimated random error.

To better see variations in the quality of the final estimate, a quality index (QI) has been defined (Huffman et al. 1997) that is approximately equivalent to the number of gauges required to produce the error in question (for the given amount of rain). The map of QI for the sample month is shown in the bottom panel of Fig. 2. In general, the land areas have a higher QI because the land areas have the gauge information in addition to that from the merged satellite estimates. Variations in QI over land are related mainly to variations in gauge density, with Europe and southeastern Australia having some of the areas of highest QI. Over the ocean the QI is higher (2–4) in the 40°N–40°S region relative to a QI of 1–2 at higher latitudes. The higher QI (lower error for the same rainfall) is due to the added sampling available with the geosynchronous satellite observations. The QI and error fields should be helpful for evaluation of research results utilizing this dataset. However, it should be remembered that the error estimates are for random error only, but include estimates of both retrieval error and sampling error.

b. Climatology

Figure 4 displays the 1979–2001 precipitation climatology map based on the GPCP Version-2 final merged product. The GPCP climatology shows the expected main features, with maxima in the Tropics in the intertropical convergence zone (ITCZ) in the Atlantic, Pacific, and Indian Oceans; in the South Pacific convergence zone (SPCZ); and over tropical Africa, South America, and the Maritime Continent between the Pacific and Indian Oceans. Dry zones in the eastern parts of the subtropical oceans are evident, as are the desert areas over land. The Pacific ITCZ is a narrow band on the Northern Hemisphere (NH) side of the equator, with peaks in both the western and eastern parts of the ocean with nearly equal values of 8.8 and 9.1 mm day^{-1}, respectively. The Atlantic Ocean ITCZ maximum is weaker and the Indian Ocean feature extends westward from Sumatra and narrows along the equator.

In the midlatitudes, the storm tracks in the Northern Hemisphere oceans are very distinct with peak values in the Atlantic and Pacific Oceans greater than in the Southern Hemisphere (SH) circumpolar storm track. A secondary maximum is evident along the northwest coast of North America from Alaska to California at the eastern end of the Pacific Ocean storm track. The Southern Hemisphere does have weak maxima southeast of Africa and South America, and a poleward extension of the SPCZ in the South Pacific Ocean. The narrow, cir-

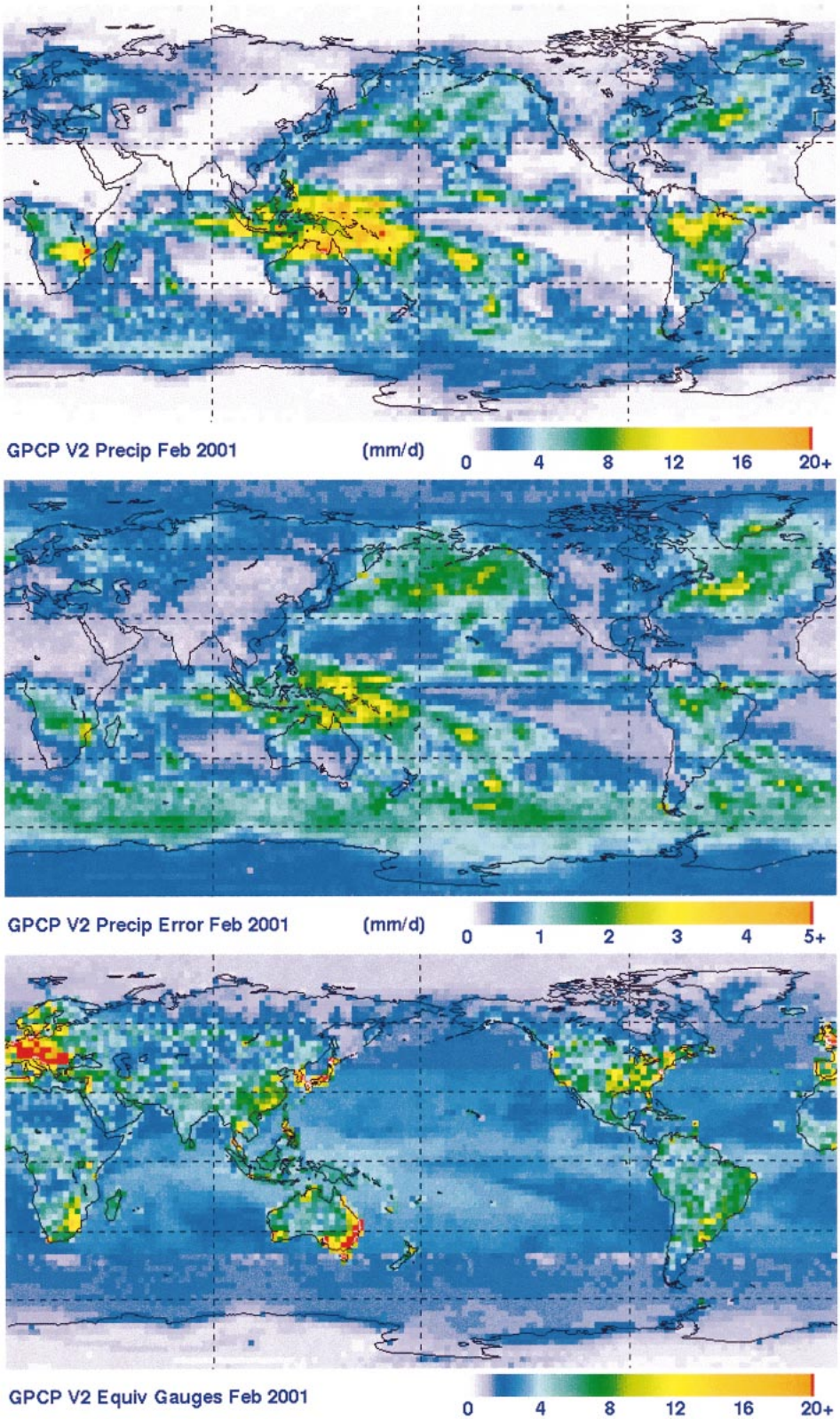

FIG. 2. SG estimates of (top) precipitation (mm day^{-1}), (middle) error (mm day^{-1}), and (bottom) quality index (equivalent gauges) for Feb 2001.

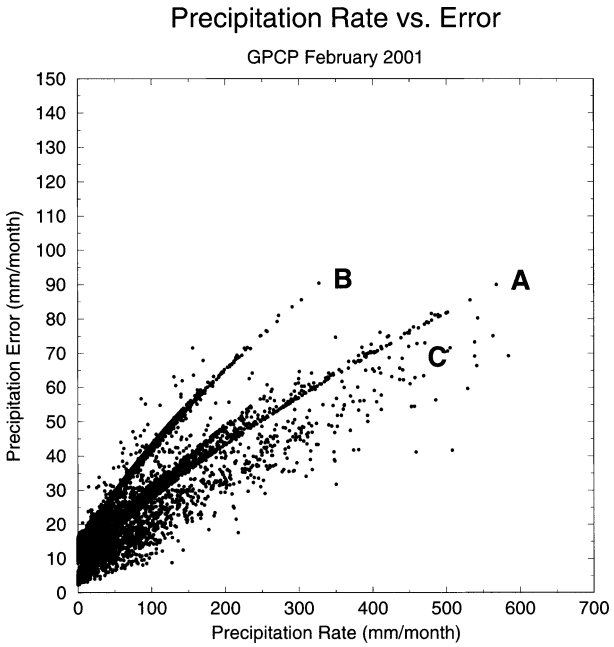

FIG. 3. Scatterplot of precipitation rate (mm month^{-1}) and error (mm month^{-1}) for Feb 2001. As described in the text; A, B, and C denote clusters of scatter.

cumpolar maximum at 65°S indicates the Southern Hemisphere storm track, but also is the latitude zone where the combination technique is transitioning from SSM/I-based precipitation estimates to TOVS-based estimates. Therefore, although the feature certainly exists, the magnitude and exact placement are more questionable than many of the other features in the climatology.

A comparison of the new Version 2 with the GPCP Version-1 climatology indicates slightly lower rainfall amounts over the tropical oceans due to a modification of the passive microwave algorithm over the ocean (Chang et al. 1995) and an increase at high latitudes (>50°) over the ocean due to the merger of the TOVS-based estimates with the SSM/I-based estimates at these latitudes.

The zonal-averaged latitudinal profile of precipitation is given in Fig. 5 for the GPCP climatology and for two conventional climatologies, from Jaeger (1976, hereafter JAE) and Legates and Willmott (1990, hereafter LW). The GPCP peak of 5.5 mm day^{-1} at 6°N is nearly the same as that from JAE. The LW peak is related to a very strong maximum shown in their climatology in the central Pacific Ocean, which is not supported by satellite observations. The GPCP curve shows a secondary tropical peak at 5°S, which appears in the other climatologies as changes in slope of the decrease from the main peak. It is tempting to interpret this secondary peak as a manifestation of a second ITCZ on the south side of the equator, but the peak is actually a composite of various ocean and land features that do not connect over any large longitudinal range (see the map in Fig. 4). The overall tropical peak in the GPCP climatology (Fig. 5) is somewhat narrower than in either of the conventional climatologies, and the subtropical minima of just below 2 mm day^{-1} are located a little equatorward of the climatologies, especially in the Southern Hemi-

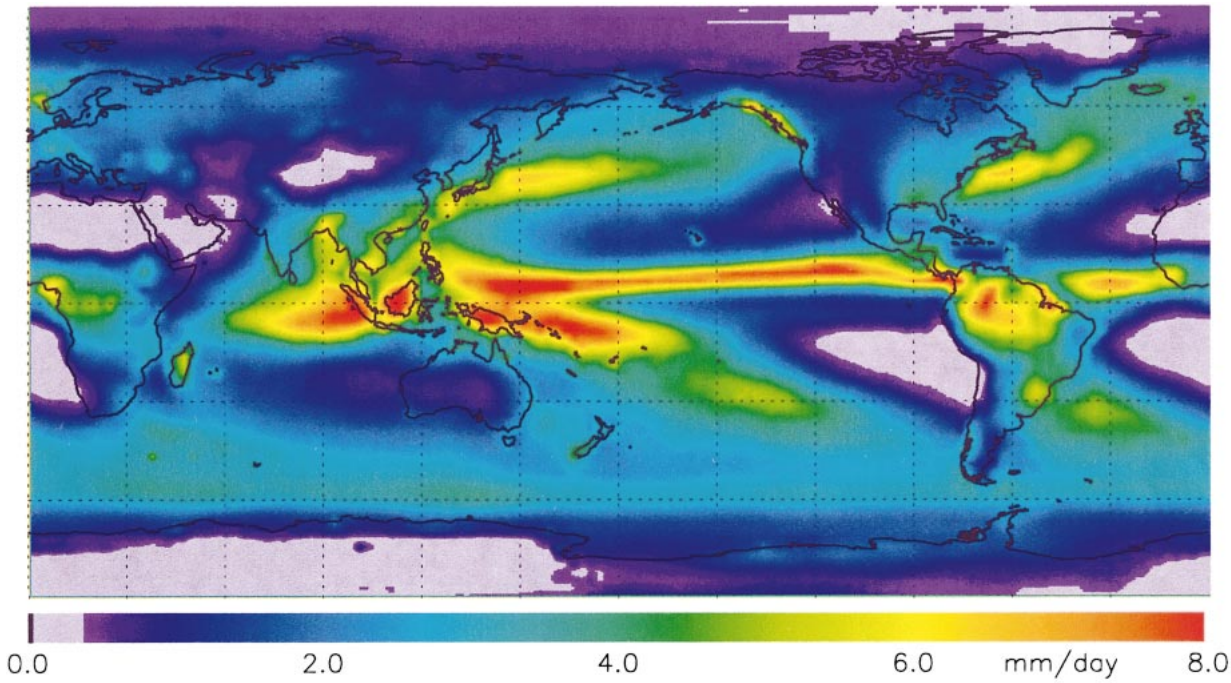

FIG. 4. The 23-yr (1979–2001) annual mean precipitation (mm day^{-1}).

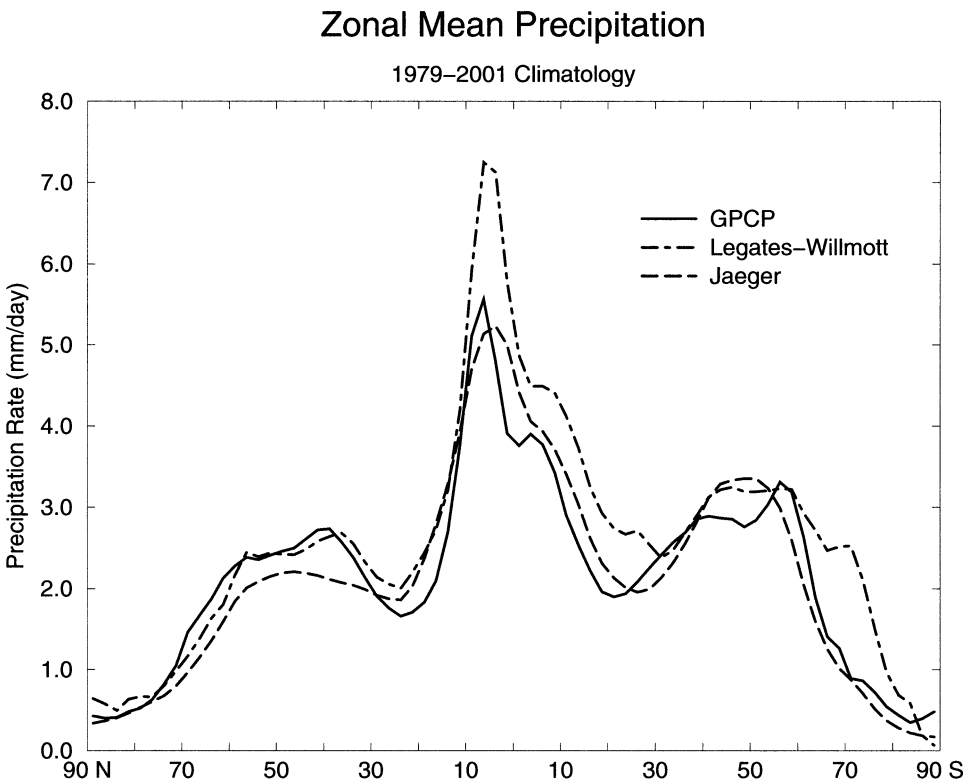

FIG. 5. Zonally averaged annual mean climatologies of precipitation (mm day^{-1}): the GPCP (solid line, see Fig. 4), Legates and Willmott (1990) (dot–dashed line), and Jaeger (1976) (long-dashed line).

sphere. The land and ocean breakdown of the latitudinal profile is shown in Fig. 6, where it can be seen the double peak exists in the ocean by itself, but that the land profile has its overall peak just south of the equator. The land peak is closer to the equator than the ocean peak.

The GPCP NH midlatitude peak is similar in magnitude and shape to that of the LW profile (Fig. 5) with higher values than the JAE profile. The main peak, at about 40°N is an oceanic peak, not showing up over land (see Fig. 6). It is mainly composed of the two oceanic storm tracks east of Asia and North America. Poleward of that peak, the GPCP curve in Fig. 5 has a weak secondary maximum at 55°N, which is clearly based over land (see Fig. 6). The LW climatology has a similar feature. The ocean profile in Fig. 6 does show a leveling off before a steep drop off to the pole. This high-latitude activity perhaps reflects a separate cyclone track at this latitude, and also the southwest-to-northeast (ocean to land) orientation of the main midlatitude rain features in the NH. From 55°N the mean precipitation decreases rapidly toward the pole dropping below 1 mm day^{-1} at 70°N. In this zone the GPCP agrees fairly well with the conventional climatologies.

In the SH the broad GPCP midlatitude maximum between 40°–60°S has two peaks, the larger being at 57°S. The exact latitude of the peaks in this zone varies among the climatologies. The distinct peak at 57°S in the GPCP field is also evident in the map in Fig. 4. As mentioned before, this zone is also where the GPCP merger technique transitions from SSM/I-based estimates to those from TOVS and because that transition is done as a function of latitude this peak, or at least the magnitude of the peak, is open to question and requires further analysis. From the midlatitude maximum the mean precipitation drops off rapidly toward the pole, similar to that of JAE. The similarities among the climatologies are encouraging, considering that they cover different periods of years. The differences, especially in the tropical oceans, are likely due to biases in the data sources.

In comparing the precipitation of the two hemispheres in Fig. 6 it is evident that the NH has more mean rainfall in the 0°–25° zone, probably due to the more extensive land mass in the NH, which in turn draws the ITCZ into the NH and also helps produce the stronger Asian monsoon in the NH. However, in the 25°–65° zone the SH has somewhat greater precipitation overall, but the NH has a greater total in this zone, if only oceans are considered. Thus, it seems that the standing waves in the NH help produce larger precipitation values over the oceans there, but the drier landmasses in this latitude zone reduce the total precipitation to slightly below the SH ocean and total values, which are nearly the same because of the relative lack of land in that zone.

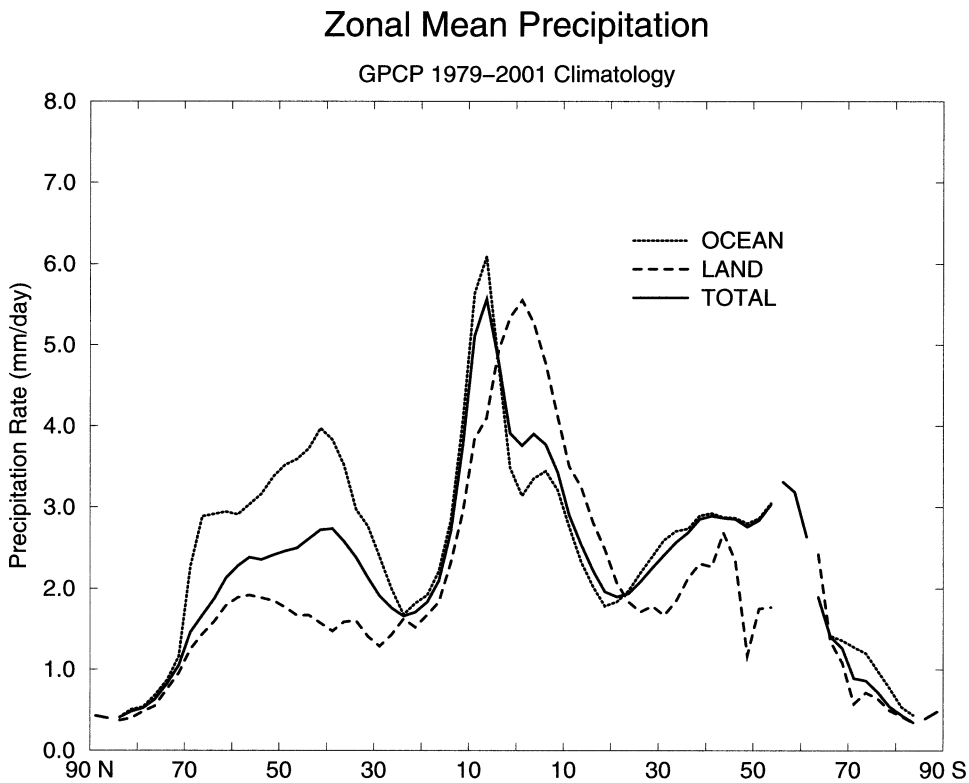

FIG. 6. Zonally averaged annual mean GPCP climatology (mm day^{-1}) (see Fig. 4): ocean-only grid blocks (dotted line), land-only grid blocks (dashed line), and the total (solid line, see Fig. 5). Gaps in the high latitudes occur when there are no land or ocean grid blocks.

TABLE 1. Upper table compares global totals for GPCP, LW; and JAE climatologies. Bottom table shows GPCP totals for different latitude bands and surface types.

	90°N–90°S avg (1979–2001)		
Surface	GPCP Version 2	LW	JAE
Ocean	2.84	3.50	2.89
Land	2.09	2.32	2.13
Total	2.61	3.13	2.65
	30°N–30°S avg (1979–2001)		
Surface	GPCP Version 2	LW	JAE
Ocean	2.94	3.80	3.08
Land	2.89	2.86	2.76
Total	2.93	3.53	2.99

	GPCP Version 2: Northern Hemisphere/Southern Hemisphere		
Surface	90°N–90°S	0°–90°N	0°–90°S
Ocean	2.84	3.17	2.62
Land	2.09	1.93	2.46
Total	2.61	2.64	2.58

	GPCP Version 2: Latitude bands			
Surface	90°–30°N	30°N–0°	0°–30°S	30°–90°S
Ocean	2.86	3.38	2.55	2.68
Land	1.58	2.53	3.35	1.06
Total	2.16	3.11	2.75	2.42

c. Global totals

Table 1 contains the global precipitation totals for the GPCP Version 2, along with those for the two conventional climatologies. For the entire globe (90°N–90°S) the GPCP total is 2.61 mm day^{-1}, comparable to the value of JAE, but lower than that of LW. However, the LW value is affected by a questionable rainfall maximum in the central Pacific Ocean (see Huffman et al. 1997 and Janowiak et al. 1995 for discussion) so that its global total value is questionable. The breakdown between ocean and land indicates higher values over ocean and because the ocean also occupies the larger area, this means that 76% of global precipitation falls over the world's oceans according to the GPCP climatology.

When the latitude band is restricted to the Tropics, that is, 30°N–30°S, the mean goes up to 2.93 mm day^{-1} and the difference between land and ocean is much smaller. The GPCP values in the Tropics are also in close agreement with those of JAE, but very different than those of LW for the aforementioned reason. As indicated in Fig. 5, the LW values appear very reasonable outside the Tropics, and even within the Tropics climate maps are similar to those of GPCP, except for the central Pacific Ocean. The GPCP Version-2 values for the Tropics are about 5% lower than the GPCP Ver-

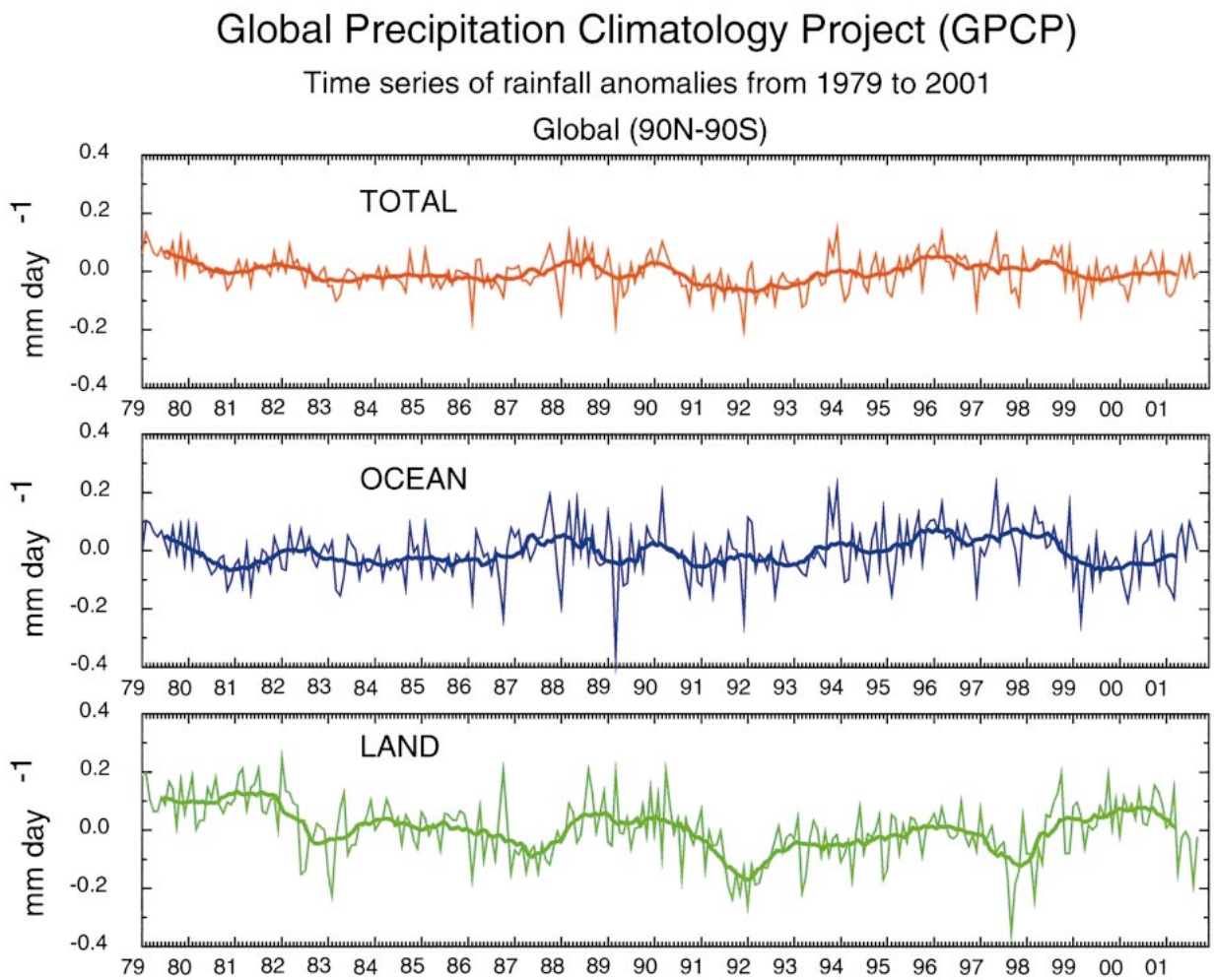

FIG. 7. Globally (90°N–90°S) averaged monthly precipitation anomalies (mm day^{-1}) for (top) total, (middle) ocean, and (bottom) land.

sion-1 means over the oceans, while over land they are nearly identical because of the influence of the rain gauges. The ocean difference is due to a modification of the microwave algorithm as mentioned earlier.

The lower part of Table 1 shows the totals for various latitude bands. When the globe is divided into the NH and SH Table 1 indicates that the NH has slightly more precipitation. When only considering oceans, the NH is still larger, but over land the SH has a higher mean precipitation rate. When the hemispheres are divided into Tropics and extratropics (bottom part of Table 1) the NH has more precipitation in the Tropics and the SH has more precipitation in the extratropics.

A time series of monthly, global anomalies from the 23-yr mean value in Table 1 is shown in Fig. 7. A 12-month running mean is also shown. The curve for land and ocean combined in the top panel indicates no noticeable trend over the observation period. This lack of a positive trend might be surprising considering predictions based on climate models of a precipitation increase associated with global warming. However, the size of the predicted increase is small and may not be detectable over a short period, such as 20 yr.

The monthly anomalies occasionally reach near a magnitude of 0.2 mm day^{-1}, but typically stay below 0.1 mm day^{-1}, a 4% variation when compared to the mean of 2.6 mm day^{-1}. The ocean and land separately have larger anomalies because of the smaller area, and the land variations are most obvious and are generally related to El Niño–Southern Oscillation (ENSO) variations. Figure 8 shows a similar diagram limited to 30°N–30°S and includes a plot of the Niño-3.4 (5°N–5°S, 120°–170°W) sea surface temperature (SST) index along with the indicators of the occurrence of major volcanic eruptions. The variations over land in the bottom panel are clearly connected to ENSO. Two major land areas in this latitude range, South America and the Maritime Continent, have dry periods during El Niño, and also the Indian summer monsoon rainfall is weaker, which results in the negative correlation between Niño-3.4 and land precipitation. A positive correlation with ocean rainfall is present, especially pronounced during

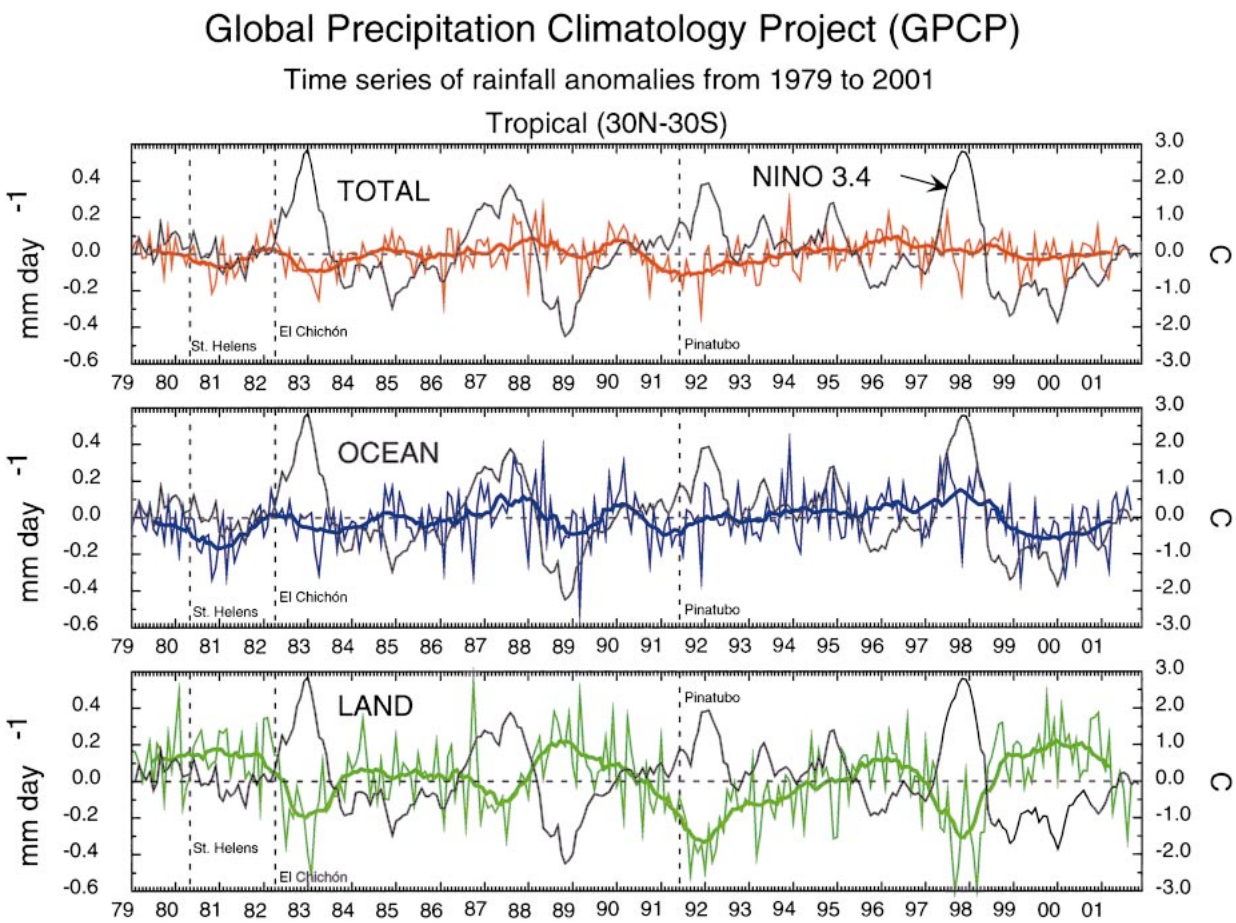

FIG. 8. Tropical (30°N–30°S) averages of monthly precipitation anomalies (mm day^{-1}) for (top) total, (middle) ocean, and (bottom) land. Vertical dashed lines indicate the months of significant volcanic eruptions. Black curves in the top, middle, and bottom panels indicate the Niño-3.4 SST index (°C).

the 1986/87 and 1997/98 El Niño events and the subsequent switches to La Niña conditions, but not so obvious with the 1982/83 and 1991/92 events. The major volcanic events also may play a role and might help to explain some decreases in precipitation and the lack of a positive ocean anomaly during the 1982 and 1992 El Niños. Research is ongoing in exploring these relations and possible causes.

d. Seasonal cycle

The evolution of the annual cycle of precipitation is seen in Fig. 9 in terms of mean maps for selected months. Figure 10 shows the zonally averaged annual cycle, separately for land and ocean and together. In tropical regions the major precipitation peaks in the Indian and Pacific Oceans, South America and the Maritime Continent are below the equator in January. In midlatitudes the NH ocean peaks are the strongest and are located further south in January. In the SH storm track the precipitation maximum is weakest. In April the western Pacific Ocean maximum is already larger north of the equator, but a double ITCZ pattern exists in the eastern Pacific Ocean. By July the precipitation in the Tropics has followed the sun northward and both the land and ocean peaks are farthest north. The NH storm tracks are weak, but the circumpolar track in the SH is at its strongest. The impact of land is in evidence in Fig. 10, which shows the mean zonally averaged annual cycle (two cycles are shown). The range of latitudes covered by the precipitation maximum during the annual cycle is clearly larger for the land areas than for the oceans, indicating the effect of the land heating at amplifying the annual cycle. In northern midlatitudes the ocean peak is clearly defined in winter at 40°N, while over land the peak is in summer, at 50°–60°N.

The regional characteristics of the seasonal cycle are given by the magnitude and phase of the first annual harmonic of precipitation seen in Fig. 11. The areas of large amplitude are associated with monsoonal regimes and shifts of the ITCZ. Shifts in phase of 180° are noted between South Asia and northern Australia, the Amazon and north coast of South America, and along the equator across the Pacific Ocean. The amplitude of the strong

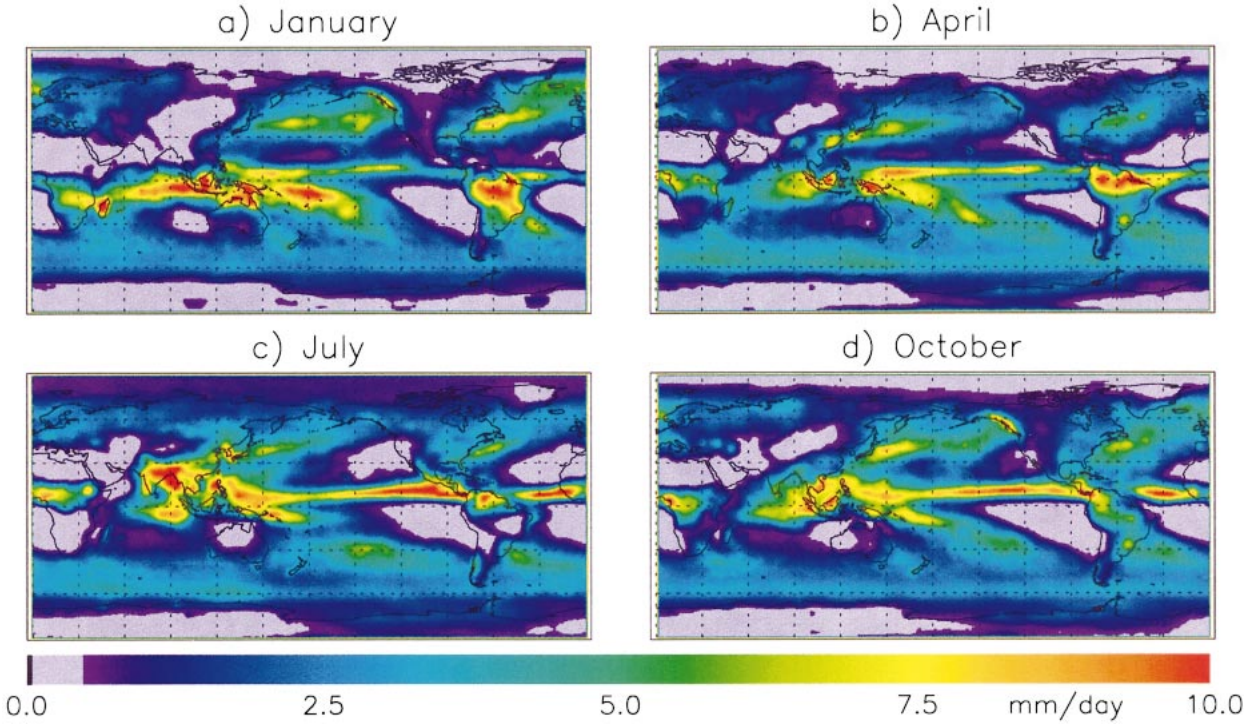

FIG. 9. The 23-yr (1979–2001) seasonal mean precipitation (mm day^{-1}) for (a) Jan, (b) Apr, (c) Jul, and (d) Oct.

feature in the eastern Pacific is partly due to the impact of tropical cyclones there in July–September. The NH midlatitude storm tracks have broad maxima with approximately a January peak. A June peak exists in the SH storm track at 50°S from south of Africa to south of Australia.

Other interesting features include a variation in the subtropical dry areas. The SH oceanic dry areas west of South America and Africa stay dry year-round, but their NH counterparts vary seasonally to a much greater degree with a relatively wet winter. The NH polar region also shows a seasonal variation with peak precipitation in the summer.

e. Example of ENSO variations

One of the most important prospective uses for any analysis of global precipitation is to examine and understand interannual changes in the distribution of large-scale precipitation and their relationship to variations in the general circulation. It has long been clear that a significant portion of the interannual variability in the large-scale atmospheric circulation is associated with the ENSO phenomenon (Bjerknes 1969; Arkin 1982; Schneider and Fleer 1989). ENSO-related changes in global precipitation, as inferred from rain gauge observations, have been presented by Ropelewski and Halpert (1987, 1989, 1996), and Janowiak and Arkin (1991); Arkin et al. (1994), and Dai and Wigley (2000) have described the ENSO signal in precipitation estimated from satellite observations. GPCP Version 2 has already been used by Curtis and Adler (2000) to create indices of ENSO based on patterns of precipitation anomalies. Their standard rainfall index, the ENSO precipitation index (ESPI), is plotted with Niño-3.4 and precipitation anomalies divided by 4.0 over the Niño-3.4 domain (Fig. 12). During the 1997/98 El Niño, ESPI led Niño-3.4, which in turn led the collocated precipitation index.

The 23-yr record contains six El Niños, including the powerful events in 1982/83 and 1997/98 (Fig. 12). An important application of GPCP is to characterize the evolution of global precipitation during ENSO over the 23-yr period, for example, in Curtis and Adler (2003), where precipitation anomaly patterns as a function of state of evolution and intensity are presented. Here we examine rain rates, anomalies, and normalized anomalies for the seasons of July–August–September (JAS) 1997, January–February–March (JFM) 1998, JAS 1998, and JFM 1999 (Fig. 13). The boreal summer of 1997 (Fig. 13a) was characterized by a reversal of the Walker circulation, as defined by the east–west precipitation gradient in the equatorial Pacific (Curtis and Adler 2000). The strongest precipitation anomalies (Fig. 13b) were confined to the equator, with increases in rainfall over much of the Pacific and decreases over the Maritime Continent, the Amazon, and Central Africa. However, normalized anomalies, ranked percentiles of rain rate based on a gamma distribution (Ropelewski and Halpert 1987), show significant changes in seasonal precipitation in the mid- to high-latitudes (Fig. 13c). A

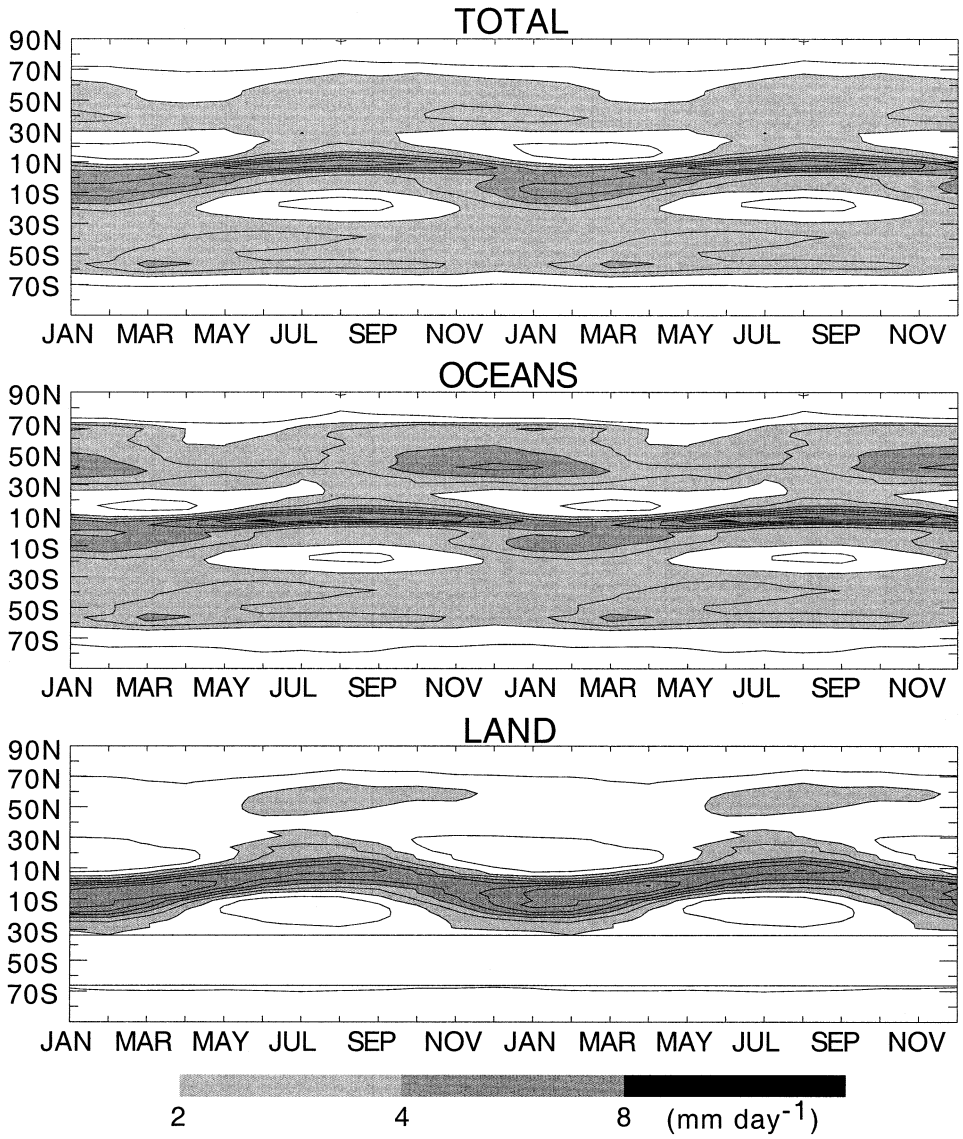

FIG. 10. Two annual cycles of zonally averaged precipitation (mm day^{-1}) over the globe (90°N–90°S) for the (top) total field, (middle) ocean only, and (bottom) land only. Contours are every 1 mm day^{-1}, beginning at 1 mm day^{-1}. Darker shading indicates greater precipitation rates. There is no appreciable land around 50°S as indicated by the lack of data there in the bottom panel.

weak La Niña emerged in the boreal summer of 1998 (Fig. 13g). A strong gradient of precipitation anomalies is seen across the Maritime Continent, with positive values southwest of Sumatra and negative values north of New Guinea (Fig. 13h). However, the normalized anomalies (Fig. 13i) do not show the global extremes observed during the El Niño. The La Niña strengthened into the beginning of 1999 (Fig. 13j). Above-normal rainfall was observed for the Maritime Continent and Amazon, but central Africa was as dry as JFM 1998 (Fig. 13k). Normalized anomalies show significantly dry conditions over the southwestern United States and southern Indian Ocean (Fig. 13l). For a detailed description of GPCP Version-2 observations of precipitation during the 1997–99 ENSO cycle, see Curtis et al. (2001).

5. Comparison with independent gauge data

The GPCP products (Version 1) have been the subject of comparison with surface rainfall data in previous studies (Huffman et al. 1997; Krajewski et al. 2000), with generally positive results. In this section the GPCP Version-2 dataset will be compared with two independent gauge datasets—one over ocean and one over land. More detailed comparison with independent surface datasets is ongoing.

In Fig. 14 the final merged GPCP product is compared

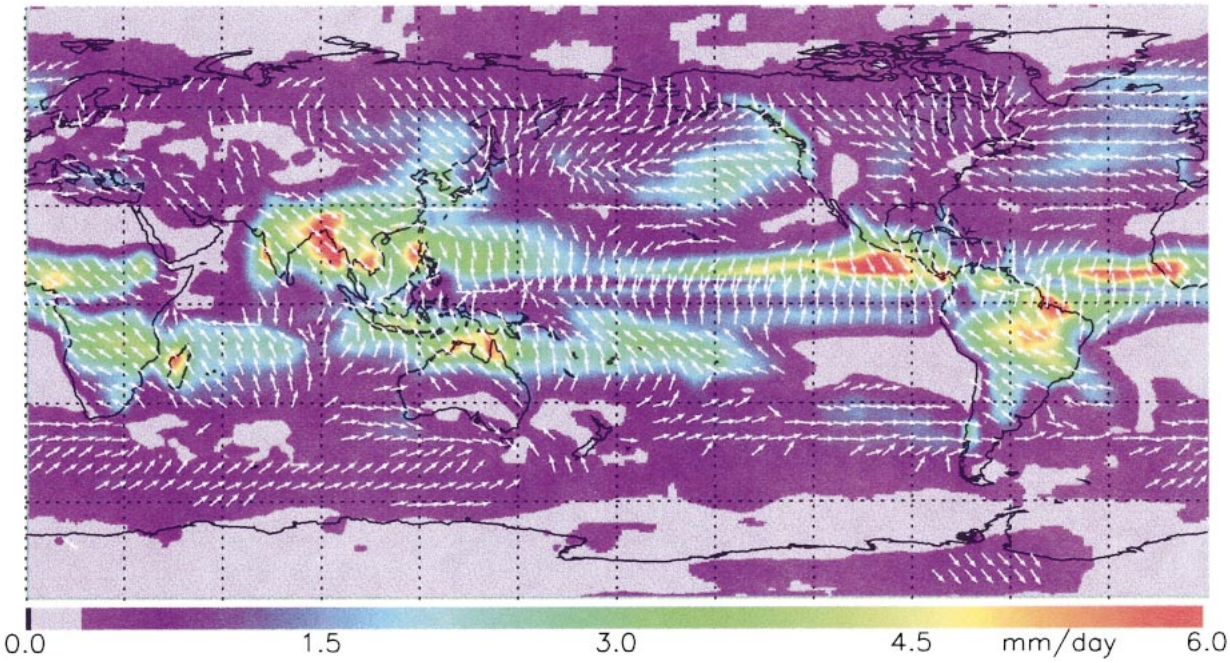

FIG. 11. The amplitude (mm day^{-1}) of the first harmonic of the average annual cycle. White arrows represent the phase (peak month) of the first harmonic, where Jan is directed to the west, Apr to the north, Jul to the east, and Oct to the south.

to the atoll rain gauge data described by Morrissey and Green (1991). The monthly GPCP-merged data do not contain the atoll data. The plot in Fig. 14 is limited to 2.5° monthly grid squares that have at least two rain gauges in the box. The plot shows significant scatter, some of which is related to how poorly a few rain gauges represent a 2.5° square. The most meaningful statistic is the bias, which is −34 mm month^{-1}, or −16%. One can see from the scatterplot that the GPCP is high compared to the atoll gauges at low values, but low compared to the atolls above about 150 mm month^{-1}. The overall difference of 16% is related to a similar difference between the ocean passive microwave technique used and the atoll gauges, because the microwave technique is used to calibrate the geosynchronous IR-based estimates. It is possible that the satellite technique is underestimating the precipitation, but there is also the possibility that the atoll gauges are not completely representative of the open-ocean precipitation. Because of this question and the fact that the atoll stations are only located in the western Pacific Ocean and are, therefore, not representative of the entire tropical ocean, the GPCP dataset has not been adjusted to take into account the difference. Additional research is ongoing to determine the representativeness of the atoll mean values.

An example of comparison of the GPCP analysis with independent gauges over land can be seen in Fig. 15. The comparison gauges are from the Oklahoma Mesonet (Brock et al. 1995) for two 2.5° grid boxes in Oklahoma. None of these gauges were used as part of the GPCP gauge analysis. The Oklahoma boxes are located just inside the 40°N boundary where both SSM/I and geosynchronous IR observations are used in the analysis. There were typically 30 Mesonet gauges located in each 2.5° GPCP grid box. This area is, therefore, subtropical to midlatitude, with an annual cycle varying from summertime thunderstorms to wintertime stratiform precipitation, including some snow.

Figure 15c shows the scatterplot for the final merged GPCP product, which includes the rain gauges as described in sections 2a(1) and 2b(1). The low bias (+1%) and high correlation indicate that the merger process and the incorporation of the gauge information has succeeded in producing a reasonable product, at least over this area. The average number of GPCP gauges used in the analysis per grid box was four. To better understand the influence of the GPCP gauge information on the resultant analysis and to estimate the quality of the GPCP analysis in areas of no or limited gauge information, Figs. 15a and 15b are shown. Figure 15a gives the scatterplot for the multisatellite analysis before any gauge information enters the analysis. The scatter is significant, although there is obvious skill and a relatively small bias (under 10%). Figure 15b shows results after an intermediate analysis step where gauges over a wide area (7.5° on a side) are used to adjust the overall satellite bias in each 2.5° grid box. The correlation increases and the bias decreases from the satellite-only case in Fig. 15a. This intermediate step can be thought of representing the case of having some gauge information available in the general area, but not many gauges in the particular analysis box. The three panels in Fig. 15, therefore, roughly represent the cases over land of (a) only satellite-based estimates, (b) satellite with a

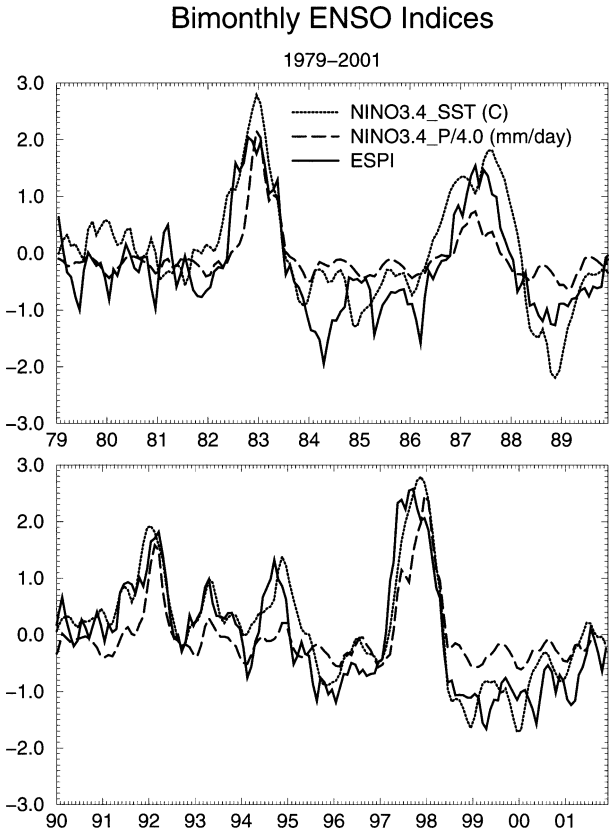

FIG. 12. Bimonthly Niño-3.4 (°C) (dotted line), precipitation anomalies averaged over the Niño-3.4 domain (mm day^{-1}) (dashed line), and ENSO precipitation index (mm day^{-1}) (solid line) for 1979–2001.

relatively poor sampling of gauges, and (c) satellite with good gauge coverage.

Another comparison with gauge information can be seen in Fig. 16, which shows the annual cycle averaged over 3 yr as seen by the GPCP product and gauge networks over two parts of Europe. The GPCP-merged satellite and gauge product uses monthly rain gauge data that are bias corrected using long-term mean monthly correction factors after Legates (1987). In Fig. 16 these estimates are compared with daily rain gauge data from high-resolution networks of the Baltic Sea Experiment (BALTEX) that have been bias corrected ''on event'' using information about precipitation type and wind speed from the individual daily synoptic data (Rubel and Hantel 2002). The annual cycles of area mean precipitation over Sweden (55°–65°N, 10°–15°E, Fig. 16a) and Poland (50°–55°N, 15°–25°E, Fig. 16b) show good agreement between GPCP Version 2 and BALTEX-corrected gauge analysis. The curves for uncorrected BALTEX data illustrate the importance of the correction for winter months.

6. Limitations

Although the GPCP monthly analysis described in this paper is a very valuable addition to the global climatology of precipitation and very useful for the study of climate variations, the dataset does have a few limitations. Because of the desire for the longest record possible and the limited length of record of the various satellites and satellite types, the record is inhomogeneous in terms of its input datasets. The basic period is mid-1987 to present that contains the SSM/I data that are used to calibrate the geosynchronous IR estimates. The earlier period is dependent on the OLR data as the main satellite input, at all latitudes. The inhomogeneity is minimized by calibrating the OLR technique during the later SSM/I period. However, the monthly maps from the earlier (OLR based) period are also smoother, that is, have weaker gradients. This dataset inhomogeneity during the period should be kept in mind when analyzing, for example, global and regional trends with this dataset.

Also, mean climatological values of precipitation over the ocean are still open to discussion, especially over middle and high latitudes. Polar latitude precipitation estimates over land also need further validation and examination. Because they are dependent on either TOVS-or OLR-based estimates, the precipitation values are a function solely of cloud information. The error fields associated with the GPCP product help the user to quantify these limitations.

It has also been shown that the GPCP analysis over land may be underestimating precipitation in some regions with orographic features (Nijssen et al. 2001). This underestimation has been examined and related mainly to the relative lack of rain gauges in mountainous regions. The density of the rain gauge data being used may not be sufficient to reliably reproduce spatial structures, even if the orographical information would be used as part of the analysis. Unfortunately the satellite observations, both passive microwave and IR, also have difficulty detecting shallow, orographic precipitation. Improvement in this area will probably require additional gauges going into the analysis and/or gauge analysis techniques that use terrain information to adjust the gauges that are available.

7. Summary and future work

A new, improved version of the Global Precipitation Climatology Project (GPCP) monthly analysis is now available and is described in this paper. The GPCP is a part of the World Climate Research Program (WCRP) and the associated Global Water Cycle and Energy Experiment (GEWEX) activity. The dataset covers the period January 1979 through the present on a monthly 2.5° latitude × 2.5° longitude grid and is globally complete using satellite and ground-based observations. The final merged product is produced a few months after real time through the data inputs and products of a number of scientists and organizations. This monthly analysis is the foundation dataset for the GPCP suite of products, which also include finer time resolution anal-

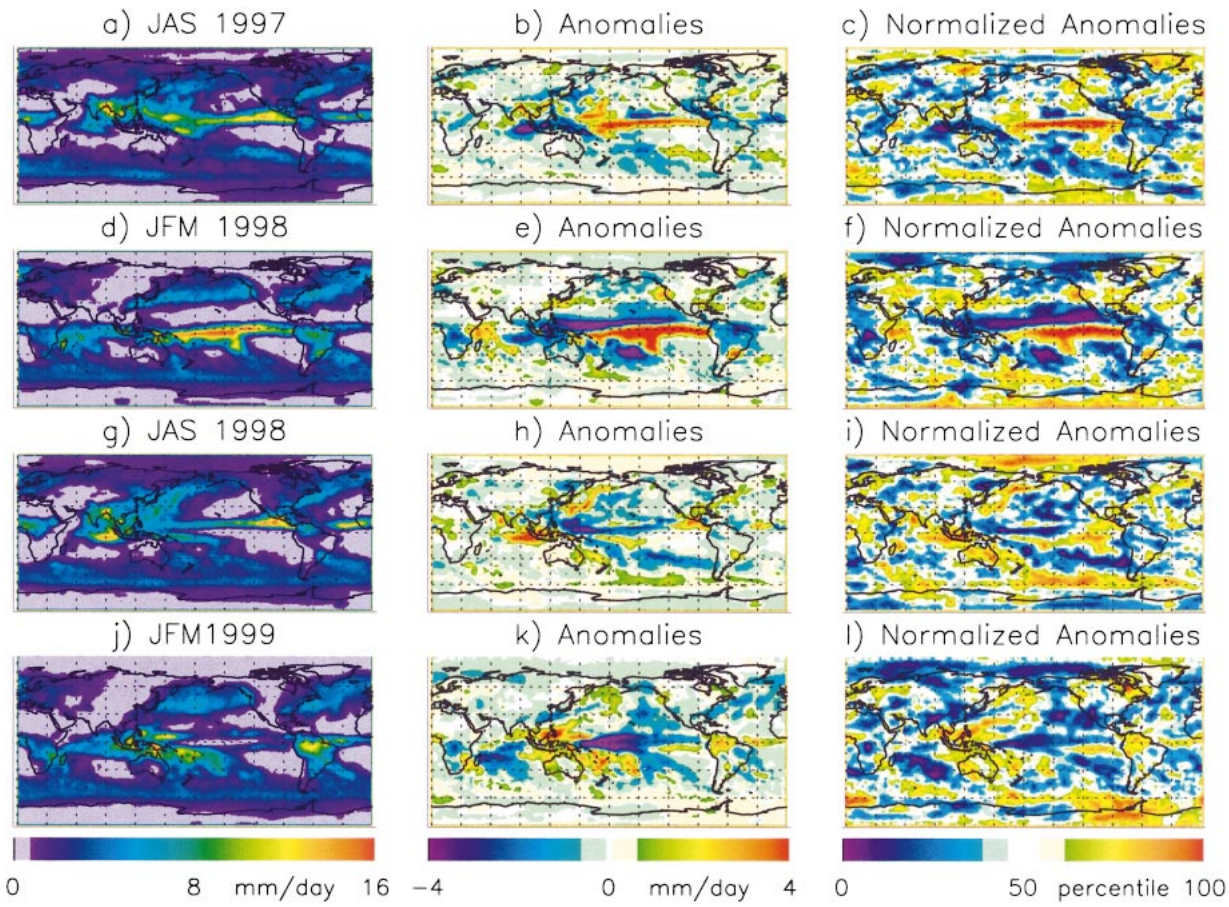

FIG. 13. The 1997–99 ENSO cycle: (a), (d), (g), and (j) precipitation rates (mm day^{-1}), (b), (e), (h), and (k) anomalies from the 1979–98 mean rates (mm day^{-1}), (c), (f), (i), and (l) normalized anomalies in percentiles of normal for JAS and JFM.

yses: a pentad analysis (Xie et al. 2002) for the full period, and a daily, global analysis from 1997 to the present (Huffman et al. 2001).

Each input and combination field in the monthly analysis is a separate product, and estimates of the random part of the error are provided with each precipitation field. These spatially and temporally varying errors allow users to assess the value of the grid values for their own application. Such applications might include validation of climate models and model-based reanalyses, calibration of hydrological models, and comparison with experimental rainfall estimation techniques.

The 23-yr (1979–2001) climatology shows the key features of the mean precipitation pattern for our planet, with an estimated mean precipitation rate of 2.6 mm day^{-1} (2.8 mm day^{-1} for oceans, 2.1 mm day^{-1} for land). The mean GPCP field compares favorably with conventional climatologies with some distinct and subtle differences. Seasonal variations are documented, including Asian and other monsoon changes along with differences between the Northern Hemisphere and Southern Hemisphere. The 23-yr record shows no noticeable increase in global or tropical precipitation during that period, although some variations in global totals over land and ocean can be related to ENSO events. The precipitation patterns and anomalies related to the 1997–99 ENSO event are also described. Because of its use of satellite data over ocean, and even over land, and the length of record, this GPCP climatology could be considered a new standard.

Comparison of the GPCP monthly values with surface gauge datasets not used in the analysis indicates that western Pacific Ocean atoll rain gauge measurements are 16% higher than the GPCP estimates. This may reflect an underestimate by the satellite-based technique in this particular area, but the representativeness of the gauge data as to open-ocean remains. Over land the comparison in Oklahoma indicates biases of 9% (satellite information only) down to 1% when the global gauge analysis is included. These values are probably typical of flat land areas, but the datasets and techniques used may lead to underestimation in some areas with orography.

The rain gauge data base at GPCC has already been expanded by additional data from up to 40 000 stations (nonreal time) and by data of the period 1979–85 (Ru-

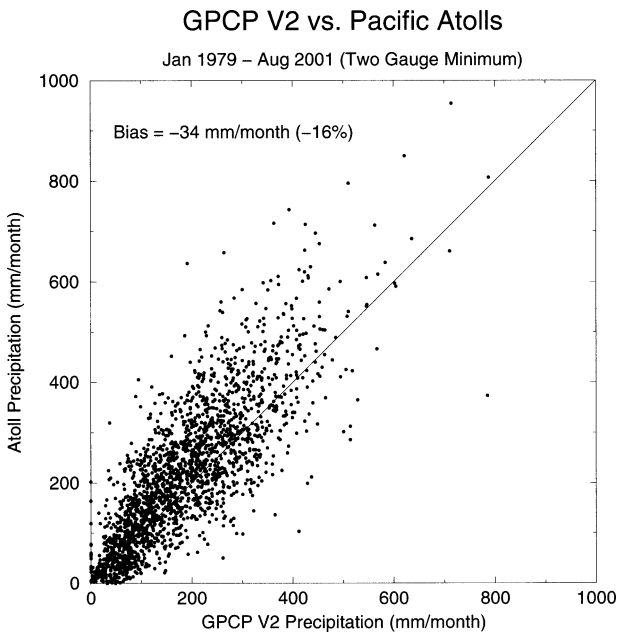

FIG. 14. Scatterplot of precipitation (mm day^{-1}) for collocated GPCP grid blocks and Pacific atoll rain gauge stations for 1979–2001.

dolf et al. 1998). Analyses based on the dense rain gauge dataset will help to estimate the bias resulting from the sparse data density and orographical structures. The bulk correction method due to systematic rain gauge measuring errors will be replaced by a new method partitioning liquid and solid precipitation (Fuchs et al. 2001).

In the future the authors and others will continue to improve the GPCP analyses for monthly and finer timescales. A key thrust of improvement will be incorporating results and data from the Tropical Rainfall Measurement Mission (TRMM), which carried the first rain radar in space and a passive microwave radiometer with the finest spatial resolution to date (Kummerow et al. 2000; Adler et al. 2003). As the TRMM algorithms mature and the length of record becomes substantial (5 yr at the end of 2002) the TRMM data will improve GPCP in a number of ways. The improved passive microwave observations along with independent radar observations on TRMM are providing the basis for improvement of passive microwave algorithms that can then be applied to the 15-yr period of SSM/I passive microwave observations. The combination of the radar and radiometer on TRMM will lead to the best instantaneous estimates available. These are already being used to calibrate and adjust other satellite information (Adler et al. 2000). One option being studied is to calibrate or adjust the GPCP monthly analyses to the TRMM-based estimates using the five or more years of overlap, and applying that calibration to the remaining years. This calibration would produce a long-period dataset with the means and other statistics of the TRMM data, at least in the Tropics between 40°N and 40°S.

TRMM data are also being used to calibrate and combine with SSM/I and geosynchronous IR data to derive 3-h resolution analyses. Precipitation information from the NOAA's Advanced Microwave Sounding Unit (AMSU) and Japan's Advanced Microwave Scanning Radiometer (AMSR), which is flying on NASA's *Aqua* and is planned for the National Space Development Agency of Japan (NASDA)'s second *Advanced Earth-Observing Satellite* (*ADEOS II*) are candidates to add to this analysis. GPCP may take advantage of these efforts and datasets to provide research-quality precipitation analyses at fine time resolution and then build the daily, pentad, and monthly fields from summation of these observations with adjustment and calibration using surface gauge and other information.

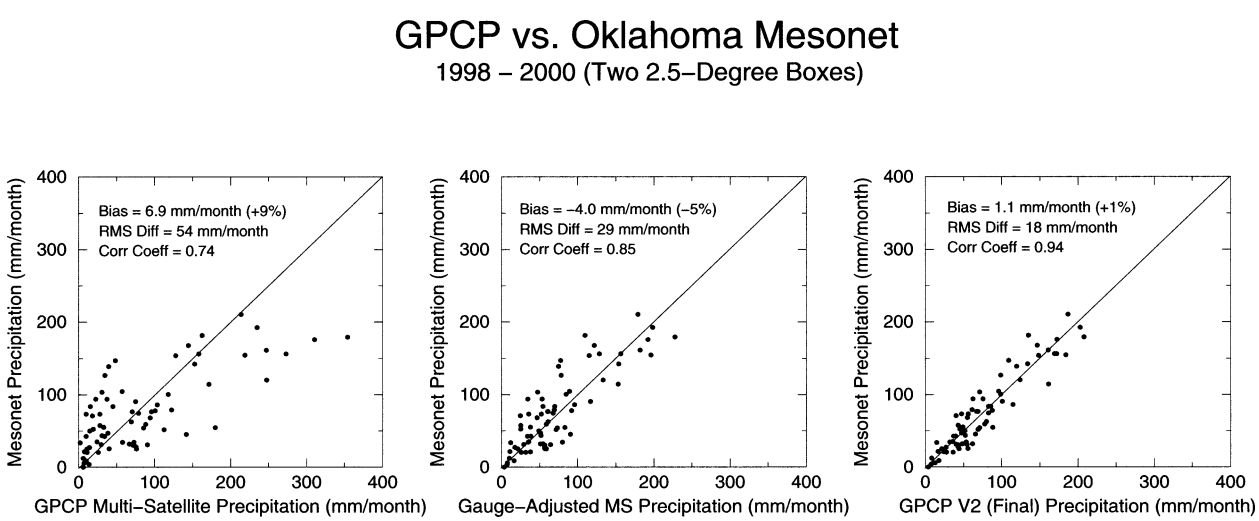

FIG. 15. Scatterplots of precipitation (mm day^{-1}) for collocated GPCP grid blocks and the OK Mesonet rain gauge stations for 1998–2000, (left) GPCP multisatellite (MS) product, (middle) MS adjusted to gauges, and (right) SG product.

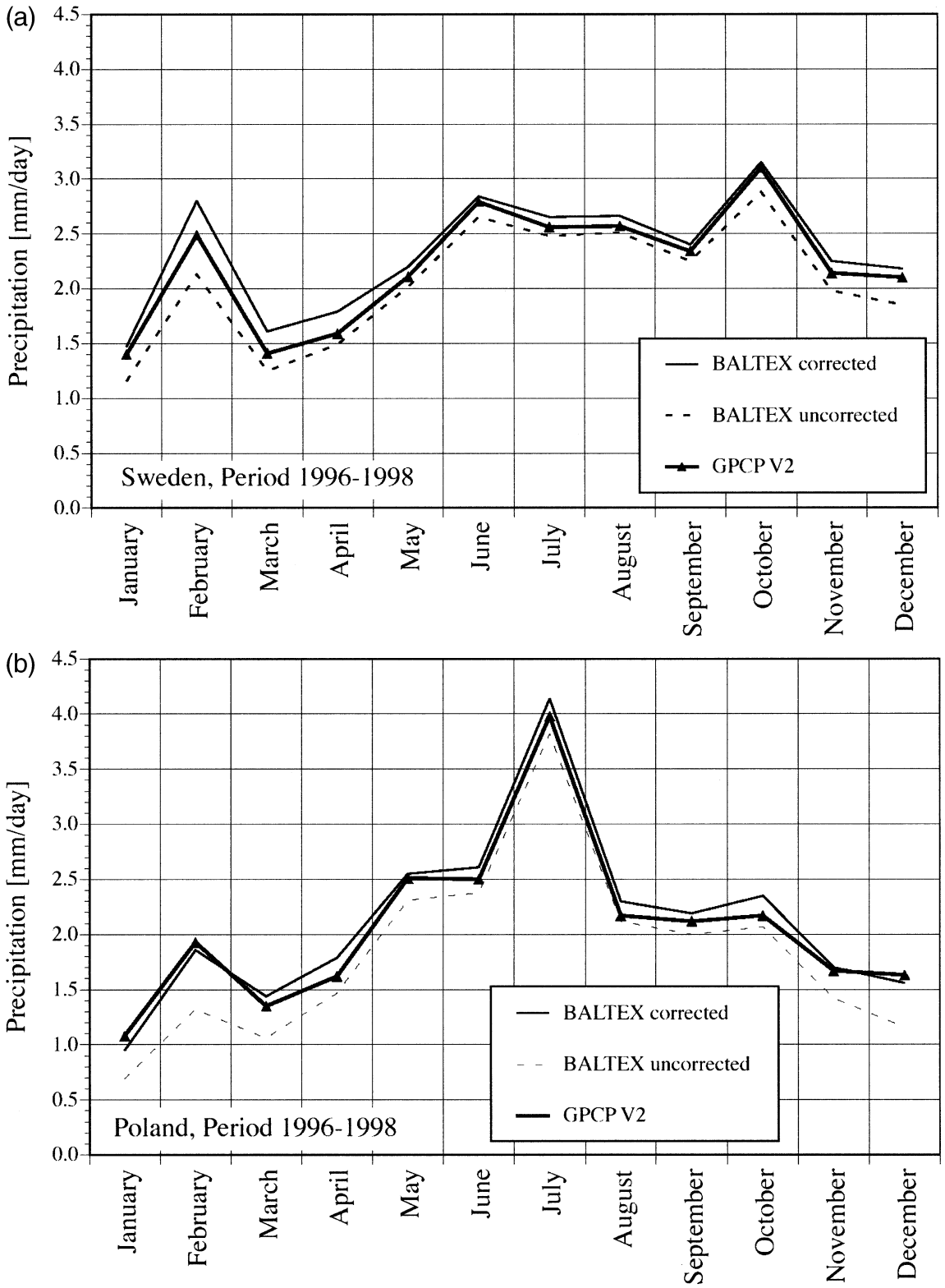

FIG. 16. Area mean precipitation (a) Sweden and (b) Poland for GPCP Version 2 versus BALTEX gauge analysis, both bias corrected and uncorrected over (a) Sweden and (b) Poland.

Acknowledgments. The GPCP Version-2 dataset is being produced by an international set of scientists and organizations. The authors thank all that have contributed data, techniques, and expertise to the effort. The geosynchronous satellite data were collected by the National Oceanic and Atmospheric Administration, Japan Meteorological Agency, European Space Agency, and EUMETSAT. Ongoing support for the activities described in this paper by Deutscher Wetterdienst, the National Aeronautics and Space Administration, and the National Oceanic and Atmospheric Administration is gratefully acknowledged.

REFERENCES

Adler, R. F., A. J. Negri, and I. M. Hakkarinen, 1991: Rain estimation from combining geosynchronous IR and low-orbit microwave data. *Global Planet. Change,* **90,** 87–92.

——, ——, P. R. Keehn, and I. M. Hakkarinen, 1993: Estimation of monthly rainfall over Japan and surrounding waters from a combination of low-orbit microwave and geosynchronous IR data. *J. Appl. Meteor.,* **32,** 335–356.

——, G. J. Huffman, and P. R. Keehn, 1994: Global rain estimates from microwave-adjusted geosynchronous IR data. *Remote Sens. Rev.,* **11,** 125–152.

——, ——, D. T. Bolvin, S. Curtis, and E. J. Nelkin, 2000: Tropical rainfall distributions determined using TRMM combined with other satellite and rain gauge information. *J. Appl. Meteor.,* **39,** 2007–2023.

——, C. Kidd, G. Petty, M. Morrissey, and H. Goodman, 2001: Intercomparison of global precipitation products: The third Precipitation Intercomparison Project (PIP-3). *Bull. Amer. Meteor. Soc.,* **82,** 1377–1396.

——, C. Kummerow, D. T. Bolvin, S. Curtis, and C. Kidd, 2003: Status of TRMM monthly estimates of tropical precipitation. *Meteor. Monogr.,* **29,** 223–234.

Arkin, P. A., 1982: The relationship between interannual variability in the 200 mb tropical wind field and the Southern Oscillation. *Mon. Wea. Rev.,* **110,** 1393–1404.

——, and B. N. Meisner, 1987: The relationship between large-scale convective rainfall and cold cloud over the Western Hemisphere during 1982–1984. *Mon. Wea. Rev.,* **115,** 51–74.

——, R. Joyce, and J. E. Janowiak, 1994: IR techniques: GOES Precipitation Index. *Remote Sens. Rev.,* **11,** 107–124.

Bjerknes, J., 1969: Atmospheric teleconnections from the equatorial Pacific. *Mon. Wea. Rev.,* **97,** 163–172.

Brock, F. V., K. C. Crawford, R. L. Elliott, G. W. Cuperus, S. J. Stadler, H. L. Johnson, and M. D. Eilts, 1995: The Oklahoma Mesonet—A technical overview. *J. Atmos. Oceanic Technol.,* **12,** 5–19.

Chang, A. T., L. S. Chiu, and G. Yang, 1995: Diurnal cycle of oceanic precipitation from SSM/I data. *Mon. Wea. Rev.,* **123,** 3371–3380.

Chiu, L., A. Chang, and J. E. Janowiak, 1993: Comparison of monthly rain rates derived from GPI and SSM/I using probability distribution functions. *J. Appl. Meteor.,* **32,** 323–334.

Curtis, S., and R. F. Adler, 2000: ENSO indices based on patterns of satellite-derived precipitation. *J. Climate,* **13,** 2786–2793.

——, and ——, 2003: Evolution of El Niño–precipitation relationships from satellites and gauges. *J. Geophys. Res.,* **108,** 4153, doi:10.1029/2002JD002690.

——, ——, G. J. Huffman, E. J. Nelkin, and D. T. Bolvin, 2001: Evolution of tropical and extratropical precipitation anomalies during the 1997–1999 ENSO cycle. *Int. J. Climatol.,* **21,** 961–971.

Dai, A., and T. M. L. Wigley, 2000: Global patterns of ENSO induced precipitation. *Geophys. Res. Lett.,* **27,** 1283–1286.

Ferraro, R. R., 1997: SSM/I derived global rainfall estimates for climatological applications. *J. Geophys. Res.,* **102,** 16 715–16 735.

——, and G. F. Marks, 1995: The development of SSM/I rain rate retrieval algorithms using ground based radar measurements. *J. Atmos. Oceanic Technol.,* **12,** 755–770.

Fuchs, T., J. Rapp, F. Rubel, and B. Rudolf, 2001: Correction of synoptic precipitation observations due to systematic measuring errors with special regard to precipitation phases. *Phys. Chem. Earth,* **B26,** 689–693.

Grody, N. C., 1991: Classification of snow cover and precipitation using the Special Sensor Microwave/Imager (SSM/I). *J. Geophys. Res.,* **96,** 7423–7435.

Gruber, A., X. J. Su, M. Kanamitsu, and J. Schemm, 2000: The comparison of two merged rain gauge–satellite precipitation datasets. *Bull. Amer. Meteor. Soc.,* **81,** 2631–2644.

Huffman, G. J., 1997: Estimates of root-mean-square random error for finite samples of estimated precipitation. *J. Appl. Meteor.,* **36,** 1191–1201.

——, and Coauthors, 1997: The Global Precipitation Climatology Project (GPCP) combined precipitation datasets. *Bull. Amer. Meteor. Soc.,* **78,** 5–20.

——, ——, M. Morrissey, D. T. Bolvin, S. Curtis, R. Joyce, B. McGavock, and J. Susskind, 2001: Global precipitation at one-degree daily resolution from multisatellite observations. *J. Hydrometeor.,* **2,** 36–50.

Jaeger, L., 1976: *Monatskarten des Niederschlags für die ganze Erde.* Bericht des Deutschen Wetterdienstes, Vol. 139, Offenbach a.M., 33 pp and plates.

Janowiak, J. E., and P. A. Arkin, 1991: Rainfall variations in the Tropics during 1986–1989. *J. Geophys. Res.,* **96,** 3359–3373.

——, ——, P. Xie, M. Morrissey, and D. Legates, 1995: An examination of the east Pacific ITCZ rainfall distribution. *J. Climate,* **8,** 2810–2823.

Joyce, R. J., and P. A. Arkin, 1997: Improved estimates of tropical and subtropical precipitation using the GOES precipitation index. *J. Atmos. Oceanic Technol.,* **14,** 997–1011.

Krajewski, W. F., G. J. Ciach, J. R. McCollum, and C. Bacotiu, 2000: Initial validation of the global precipitation climatology project monthly rainfall over the United States. *J. Appl. Meteor.,* **39,** 1071–1086.

Kummerow, C., and Coauthors, 2000: The status of the Tropical Rainfall Measuring Mission (TRMM) after two years in orbit. *J. Appl. Meteor.,* **39,** 1965–1982.

Legates, D. R., 1987: A climatology of global precipitation. *Publ. Climatol.,* **40**, 85 pp.

——, and C. J. Willmott, 1990: Mean seasonal and spatial variability in gauge-corrected, global precipitation. *Int. J. Climatol.,* **10,** 111–127.

Li, Q., R. Ferraro, and N. C. Grody, 1998: Detailed analysis of the error associated with the rainfall retrieved by the NOAA/NESDIS SSM/I Rainfall Algorithm: Part I. Tropical oceanic rainfall. *J. Geophys. Res.,* **103,** 11 419–11 427.

——, ——, and ——, 2000: Adequacy of using a 1/3-degree Special Sensor Microwave Imager dataset to estimate climate-scale rainfall. *J. Appl. Meteor.,* **39,** 680–685.

McCollum, J. R., A. Gruber, and M. Ba 2000: Discrepancy between gauges and satellite estimates of rainfall in equatorial Africa. *J. Appl. Meteor.,* **39,** 666–679.

——, R. Ferraro, M. B. Ba, and W. F. Krajewski, 2002: Validation and intercomparison of satellite rainfall estimation algorithms over the continental United States. *J. Appl. Meteor.,* **41,** 1065–1080.

Morrissey, M. L., and J. S. Green, 1991: The Pacific atoll raingauge data set. University of Hawaii, Planetary Geoscience Division Contribution 648, 45 pp.

Nijssen, B., G. M. O'Donnell, D. P. Lettenmaier, D. Lohmann, and E. F. Wood, 2001: Predicting the discharge of global rivers. *J. Climate,* **14,** 3307–3323.

Ropelewski, C. F., and M. S. Halpert, 1987: Global and regional-

scale precipitation patterns associated with the El Niño/Southern Oscillation. *Mon. Wea. Rev.,* **115,** 1606–1626.

——, and ——, 1989: Precipitation patterns associated with the high index phase of the Southern Oscillation. *J. Climate,* **2,** 268–284.

——, and ——, 1996: Quantifying Southern Oscillation–precipitation relationships. *J. Climate,* **9,** 1043–1059.

Rubel, F., and M. Hantel, 2002: BALTEX 1/6-degree daily precipitation climatology 1996–1998. *Meteor. Atmos. Phys.,* **77,** 155–166.

Rudolf, B., 1993: Management and analysis of precipitation data on a routine basis. *Proc. Int. WMO/IAHS/ETH Symp. on Precipitation and Evaporation, Bratislava, Slovakia,* Slovak Hydrometeorological Institute, 69–76.

——, H. Hauschild, W. Rüth, and U. Schneider, 1994: Terrestrial precipitation analysis: Operational method and required density of point measurements. *Global Precipitation and Climate Change,* M. Desbois and F. Desalmand, Eds., NATO ASI Series I, Vol. 26, Springer–Verlag, 173–186.

——, T. Fuchs, W. Rueth, and U. Schneider, 1998: Precipitation data for verification of NWP model re-analyses: The accuracy of observational results. *Proc. WCRP Int. Conf. on Reanalyses,* Washington, DC, WCRP, WMO/TD-No. 876, WCRP-104, 215–218.

Schneider, U., and H. E. Fleer, 1989: Development of sea surface temperature, surface wind and divergence anomalies during a composite ENSO episode. *Theor. Appl. Climatol.,* **39,** 146–159.

Sevruk, B., 1989: Reliability of precipitation measurements. *Proc. WMO/IAHS/ETH Workshop on Precipitation Measurements,* St. Moritz, Switzerland, World Meteorological Organization, 13–19.

Susskind, J., and J. Pfaendtner, 1989: Impact of interactive physical retrievals on NWP. *Report on the Joint ECMWF/EUMETSAT Workshop on the Use of Satellite Data in Operational Weather Prediction: 1989–1993,* T. Hollingsworth, Ed., Vol. 1, ECMWF, 245–270.

——, P. Piraino, L. Rokke, T. Iredell, and A. Mehta, 1997: Characteristics of the TOVS Pathfinder Path A dataset. *Bull. Amer. Meteor. Soc.,* **78,** 1449–1472.

Ungersböck, M., F. Rubel, T. Fuchs, and B. Rudolf, 2000: Bias correction of global daily rain gauge measurements. *Phys. Chem. Earth,* **B26,** 411–414.

Wilheit, T., A. Chang, and L. Chiu, 1991: Retrieval of monthly rainfall indices from microwave radiometric measurements using probability distribution functions. *J. Atmos. Oceanic Technol.,* **8,** 118–136.

Wilmott, C. J., C. M. Rowe, and W. D. Philpot, 1985: Small-scale climate maps: A sensitivity analysis of some common assumptions associated with grid-point interpolation and contouring. *Amer. Cartographer,* **12,** 5–16.

Xie, P., and P. A. Arkin, 1997: Global precipitation: A 17-year monthly analysis based on gauge observations, satellite estimates, and numerical model outputs. *Bull. Amer. Meteor. Soc.,* **78,** 2539–2558.

——, and ——, 1998: Global monthly precipitation estimates from satellite-observed outgoing longwave radiation. *J. Climate,* **11,** 137–164.

——, B. Rudolf, U. Schneider, and P. A. Arkin, 1996: Gauge-based monthly analysis of global land precipitation from 1971 to 1994. *J. Geophy. Res.,* **101,** 19 023–19 034.

——, J. E. Janowiak, P. A. Arkin, R. F. Adler, A. Gruber, R. Ferraro, G. J. Huffman, and S. Curtis, 2003: GPCP pentad precipitation analyses: An experimental dataset based on gauge observations and satellite estimates. *J. Climate,* **16,** 2197–2214.